

Predicting burst events in a forced 2D flow: A wavelet-based analysis

Anagha Madhusudanan^{2,3}† and Rich R. Kerswell¹

¹ Department of Applied Mathematics and Theoretical Physics, Centre for Mathematical Sciences, Wilberforce Road, Cambridge CB3 0WA, UK

² Isaac Newton Institute for Mathematical Sciences, CB3 0EH, Cambridge, UK

³ Department of Aerospace Engineering, Indian Institute of Science, Bangalore, India

(Received xx; revised xx; accepted xx)

1. Abstract

Predicting and perhaps mitigating against rare, extreme events in fluid flows is an important challenge. Due to the time-localized nature of these events, Fourier-based methods prove inefficient in capturing them. Instead this paper uses wavelet-based methods to understand the underlying patterns in a forced flow over a 2-torus which has intermittent high-energy burst events interrupting an ambient low energy ‘quiet’ flow. Three methods are examined to predict burst events: (1) a straightforward energy tracking approach which acts as the benchmark; (2) a wavelet proper orthogonal decomposition (WPOD) which uncovers the key flow patterns seen in the quiet regions and the bursting episodes; and (3) a wavelet resolvent analysis (WRA) that reveals the forcing structures that amplifies the underlying flow patterns. Both the wavelet-based approaches succeed in producing better (earlier) predictions than a simple energy criterion, with the WRA-based technique always bettering WPOD. However, both also produce false positives and the improvement of the WRA approach over WPOD is not as substantial as anticipated. We conjecture that this is because the mechanism for the bursts in the flow studied is found to be largely modal associated with the unstable eigenfunction of the Navier-Stokes operator linearized around the mean flow. The forcing approach should deliver much better improvements over the WPOD approach for generically non-modal bursting mechanisms where there is a lag between the imposed forcing and the final response pattern.

2. Introduction

Intermittent extreme events, characterised by a sudden increase in observables like energy or dissipation, are frequently encountered in both natural and engineering fluid flow systems. Some examples include extreme weather events (e.g. Neelin *et al.* 1998), rogue waves in the ocean (e.g. Dysthe *et al.* 2008) and high dissipation events in turbulent flows (e.g. Yeung *et al.* 2015; Chandler & Kerswell 2013). These events can have significant impacts. Understanding the mechanisms that generate such events, and predicting them, are therefore active areas of research (Farazmand & Sapsis 2019*b*; Sapsis 2021).

For instance, Donzis & Sreenivasan (2010) analysed direct numerical simulation (DNS) data to identify the observables that act as precursors to the intermittent events. In another work, Babaee & Sapsis (2016) used data to identify time-dependent orthonormal bases that characterise the transient instabilities in a system, which were then used

† Email address for correspondence: anaghamadhu91@gmail.com

to forecast extreme events (Farazmand & Sapsis 2016). However, working with time-dependent modes can become computationally expensive and therefore a variational framework that identified static structures responsible for the extreme events was formulated by Farazmand & Sapsis (2017, 2019b). By tracking these identified structures, methods to predict and control the burst events was introduced (Farazmand & Sapsis 2019a; Blonigan *et al.* 2019). A graph theoretic approach that uses clustering algorithms to find a hierarchy of coherent structures in intermittent flows have been used (Schmid *et al.* 2018). More recently, the use of machine learning to identify and control extreme events has also gained popularity (e.g. Wan *et al.* 2018; Guth & Sapsis 2019; Pyragas & Pyragas 2020; Qi & Majda 2020; Doan *et al.* 2021; Racca & Magri 2022; Rudy & Sapsis 2022; Fox *et al.* 2023). Another method, and one that is of more direct relevance to the current work, is the use of a variation of proper orthogonal decomposition (POD), called conditional-POD, to identify the dominant structures that are responsible for intermittent events (Schmidt & Schmid 2019).

Due to the time-localised nature of intermittent events, the Fourier basis is generally inefficient at characterising them. Wavelets are better adapted for this purpose, which suggests that wavelet-based methods could potentially provide another class of techniques for understanding and predicting intermittent events. Wavelets have found application in the analysis of turbulent signals since the early 1900s (e.g. Farge & Rabreau 1988; Meneveau 1991; Farge 1992). Since then they have found varied applications in turbulence such as, for instance, extraction of the coherent and incoherent parts of a turbulent flow-field (e.g. Farge *et al.* 2001, 2003) and development of simulation methods using wavelet-based numerical algorithms and turbulence models (see review by Schneider & Vasilyev (2010)) etc. Wavelet coefficients have also been used for detecting pipe bursts in water distribution systems (Srirangarajan *et al.* 2013) and predicting rouge waves (Bayındır 2016). Data-driven decomposition techniques based on wavelets have been introduced by Floryan & Graham (2021) to generate a hierarchical orthogonal basis from a flow and by Ren *et al.* (2021) to extract the different dominant scales in a flow. Recent studies by Gupta *et al.* (2022) and Barthel & Sapsis (2023) have used wavelet analysis along with POD for identifying coherent structures in intermittent flows. In a parallel line of work, the extensively used resolvent analysis technique has been extended to incorporate a temporal wavelet basis. This modification, demonstrated by Ballouz *et al.* (2023a) in their study of transient energy growth in a channel and by Ballouz *et al.* (2023b) to model statistically non-stationary flows, broadens the scope of resolvent analysis.

In the current work, we aim to contribute towards understanding and predicting intermittent high-energy events in fluid flows by employing wavelet-based methods. A two-dimensional (2D) Kolmogorov flow at a Reynolds number of 40, forced by a sinusoidal body force with wavenumber 4, is considered. This flow is temporally characterised by a persistent quiet region that is intermittently interrupted by high-energy burst events (e.g. Chandler & Kerswell 2013; Page *et al.* 2021). To understand the temporal characteristics of the flow, we first project it onto a wavelet basis. Two wavelet-based methods will be used to analyse the flow: (1) Wavelet-based Proper Orthogonal Decomposition (WPOD) to distinguish the dominant flow patterns of the quiet region and burst events and (2) Wavelet-based Resolvent Analysis (WRA) to identify forcing structures that generate the quiet region and burst events. The identification of these flow patterns prompts a subsequent question: can these patterns be utilised to predict oncoming burst events? We will therefore explore whether tracking the flow patterns obtained from WPOD (prediction method 2) and from WRA (prediction method 3) enables prediction of oncoming burst events. The predictions will be compared to those obtained from the more straightforward approach of just tracking the energy of the

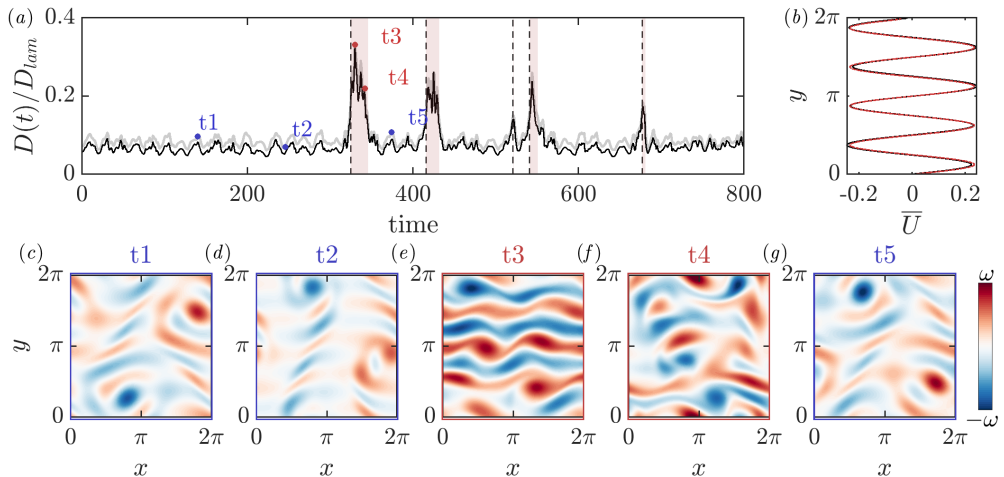


Figure 1: (a) The time-series of $D(t)/D_{lam}$ from the full data is shown in grey and for $k_x = 0, 1, 2, 3$ is shown in black, for a sample time interval. Predictions of the burst event obtained using the energy tracking-based method 1 are also shown, with the red-shaded regions, where $D(t)/D_{lam} > 0.15$, defined as the burst event, and dashed black vertical lines indicating the predictions of the burst events. (c-g) The vorticity field at the five time instances $t1$ - $t5$ indicated on (a) are also shown, where the contours indicate negative (red) and positive (blue) vorticity, respectively. The colour limits are kept the same across the five time snapshots. In (b) the mean profile obtained from the data (black line) is compared to the symmetrized mean profile (red line).

flow (prediction method 1). We find that both methods 2 and 3 do better predict the burst events, but with only marginal improvements over the predictions from method 1. Normal-mode mechanisms likely being the cause for energy-amplification in this flow could potentially explain this prediction performance.

The outline of the rest of this manuscript is as follows. 2D Kolmogorov flow is introduced in §3, and §3.3 shows how predictions of oncoming burst events can be obtained by tracking the energy of the flow (prediction method 1). The aim thereafter is to decompose the flow into the quiet regions and the intermittent burst events. The efficiency of the wavelet basis in achieving such a decomposition is shown in §5, and this is compared to the efficiency of the Fourier basis in §4. Thereafter, in §6 and §7, we probe the underlying flow patterns in this intermittent flow using WPOD. Predictions of the burst events obtained by tracking these WPOD modes (prediction method 2) are then studied in §8. Following this, in §9 we use WRA to distinguish the structures that force the quiet regions and burst events. Predictions obtained from tracking these forcing structures (prediction method 3) are then compared to those obtained from methods 1 and 2 in §10. Following this, we will briefly discuss the different predictions performances in §11 and then a final discussion follows in §12.

3. 2D Kolmogorov flow

The intermittent flow that we will use as our example in this work is the incompressible 2D Kolmogorov flow. The two dimensions are denoted by x and y , respectively. The domain is doubly periodic with size L_x in the x -direction and L_y in the y -direction. The flow is forced in the x -direction by a sinusoidal body forcing of the form $\zeta \sin(2\pi n y^*/L_y)$

($(\cdot)^*$ indicates dimensional quantities), where ζ is the amplitude of the forcing per unit mass of fluid and n is the wavenumber of the forcing. The mean-velocity is $U(y)\hat{\mathbf{i}}$, where $(\hat{\mathbf{i}}, \hat{\mathbf{j}})$ are unit vectors in the (x, y) directions. The mean is here defined over the x -direction and time. Additionally, it is symmetrized in the wall-normal direction (why such a symmetrization is required is discussed in §3.2). The fluctuations of velocities around this mean are denoted by u and v in the x and y directions, respectively. Pressure is denoted by p and time by t . The length-scale $L_y/2\pi$ and time-scale $\sqrt{L_y/2\pi}\zeta$ is used to non-dimensionalize the system. The non-dimensional number that characterise this system is the Reynolds number defined as $Re := (\sqrt{\zeta}/\nu)(L_y/2\pi)^{(3/2)}$. Here we consider a flow with $n = 4$, $Re = 40$ and $L_x = L_y = 2\pi$, which is a regime characterised by intermittent burst events as will be discussed in §3.3.

The non-dimensional equations linearized around the mean state $(U(y), 0)$ are:

$$\frac{\partial \mathbf{u}}{\partial t} + U \frac{\partial \mathbf{u}}{\partial x} + v \frac{\partial U}{\partial y} \hat{\mathbf{i}} + \nabla p - \frac{1}{Re} \nabla^2 \mathbf{u} = \underbrace{\overline{\mathbf{u} \cdot \nabla \mathbf{u}} - \mathbf{u} \cdot \nabla \mathbf{u}}_{\mathbf{f}}, \quad \nabla \cdot \mathbf{u} = 0, \quad (3.1)$$

where $\mathbf{u} = (u, v)$. The non-linear terms of the equation $\overline{\mathbf{u} \cdot \nabla \mathbf{u}} - \mathbf{u} \cdot \nabla \mathbf{u}$ are hereafter represented by a forcing term $\mathbf{f} = (f_x, f_y)$ where f_x and f_y represent the forcing to the x and y momentum equations, respectively.

Using the incompressibility condition and taking the curl of (3.1), we rewrite (3.1) in vorticity (ω) form as:

$$\frac{\partial \omega}{\partial t} + \left[U \frac{\partial}{\partial x} - \frac{1}{Re} \Delta - U'' \Delta^{-1} \frac{\partial}{\partial x} \right] \omega = F, \quad (3.2)$$

where $\omega := \partial v / \partial x - \partial u / \partial y$ and $F := \partial f_y / \partial x - \partial f_x / \partial y$. Let us consider a Fourier transform in the homogeneous x -direction. The one-dimensional (1D) discrete Fourier transform of ω gives

$$\omega(x, y, t) = \sum_{k_x = -(N_x/2)}^{(N_x/2)} \tilde{\omega}(y, t; k_x) e^{ik_x x}, \quad (3.3)$$

where $\tilde{\cdot}$ represents the 1D Fourier transform, k_x is the streamwise wavenumber non-dimensionalised by $L_y/2\pi$ and N_x is the number of grid-points used to discretize the x -direction. Similarly, \tilde{F} is the 1D Fourier transform of F . Using the Fourier transforms, we obtain the following linear equation:

$$\dot{\tilde{\omega}}(y, t; k_x) + \mathbf{A} \tilde{\omega}(y, t; k_x) = \tilde{F}(y, t; k_x), \quad (3.4)$$

where $(\dot{\cdot})$ denotes the derivative in time. The matrix \mathbf{A} contains the finite-dimensional discrete approximations of the linearized momentum equation from (3.2) in terms of the 1-D Fourier transforms. The derivatives $(\partial/\partial x, \partial/\partial y)$ have been replaced with $(ik_x, \partial/\partial y)$.

3.1. Direct Numerical Simulation data

Direct numerical simulation (DNS) data for the Kolmogorov flow at $Re = 40$ and $n = 4$ is obtained using the code from Chandler & Kerswell (2013). The DNS was run on a grid with $N_x = 256$ points in the x -direction and $N_y = 257$ points in the y -direction. Figure 1(a) shows the time series of total dissipation $D(t) := \langle \omega, \omega \rangle_{x,y}$ normalised by the laminar dissipation rate $D_{lam} := Re/(2n^2)$. Here $\langle a, b \rangle_{x,y}$ denotes the inner product $\int_0^{L_x} \int_0^{L_y} b^*(x, y, t) a(x, y, t) dx dy$. The time series represented by the grey line is obtained from the full dataset. On the other hand, the time series in black is obtained by retaining only the smallest streamwise wavenumbers with $|k_x| \leq 3$. The black line follows the grey

line reasonably well, thereby suggesting that the $|k_x| \leq 3$ modes are responsible for the dominant dynamics in the flow. Example snapshots of the flow at the five times denoted in figure 1(a) is shown from figure 1(c-g), where the red and blue contours represent the positive and negative vorticity fluctuations, respectively. Here again we observe the presence of large-scale structures in the flow, further confirming that the smallest wavenumbers dominate the flow dynamics. This is consistent with the observations in Page *et al.* (2021). For the rest of this manuscript, we will therefore project the full DNS data onto the $|k_x| \leq 3$ modes, and use the truncated data for the POD and resolvent-based analyses. This truncation using a Fourier transform is not essential for the work that follows, but just allows us to expedite the computations.

3.2. Symmetrization of the mean profile

Let us briefly consider the mean velocity profiles $U(y)$ obtained from this flow, where the mean is defined over the x -direction and time. The converged mean profiles from this flow is expected to follow two symmetries: (i) a shift-and-reflect symmetry $\mathcal{S} : U(y) \rightarrow -U(y + \pi/4)$ and (ii) a rotational symmetry $\mathcal{R} : U(y) \rightarrow -U(-y)$. Chandler & Kerswell (2013) investigated the mean profiles obtained using 10^5 time units of the flow, and observed that even this was not long enough to obtain a converged mean profile. The black line (which is asymmetric when investigated closely) in figure 1(b) represents the mean computed from 16800 snapshots of data. This obtained mean does not follow the symmetries. Therefore, as done in Chandler & Kerswell (2013), we will here use a symmetrized mean profile $U(y)$ which is extracted from the asymmetric mean obtained from DNS $U_a(y)$ as

$$U(y) := \frac{1}{2n} \sum_{m=0}^{2n-1} \mathcal{S}^{-m} U'(\mathcal{S}^m y), \text{ where } U' := \frac{1}{2} [U_a(y) + \mathcal{R}^{-1} U_a(\mathcal{R}y)]. \quad (3.5)$$

Here $n = 4$. The red line in figure 1(b) shows $U(y)$, and this symmetrised mean will be used for the rest of this work.

3.3. Predicting burst events using variance - Method 1

Before moving on to the wavelet-based techniques for understanding and predicting burst events, let us here consider the most straightforward approach to predicting the burst events. This involves simply tracking the variance of the flow, and identifying times where the variance crosses a threshold value. For the 2D Kolmogorov flow, if we define the burst events as times when $D(t)/D_{lam} > 0.15$ (Page *et al.* 2021), the red-shaded regions in figure 1(a) indicate the burst events. The vertical black dashed lines indicate the beginning of these burst events, and therefore represent the prediction times obtained using this method. These will be the benchmark predictions to improve upon.

4. Decomposing the flow: Fourier bases

Our first objective is to distinguish flow patterns that exist in the quiet region and the burst events. To identify such structures, it is necessary to decompose the flow into components corresponding to the quiet region and the burst events. In this section, we will use the Fourier basis for this decomposition. Looking ahead, isolating the time-localised burst events using the global Fourier basis may prove to be inefficient. Therefore, the aim of this section is to provide motivation for moving towards using a wavelet basis.

We are interested in analysing a burst event, and require multiple realisations of such events. Consider N_e realisations of the burst event, each containing N_t time-snapshots

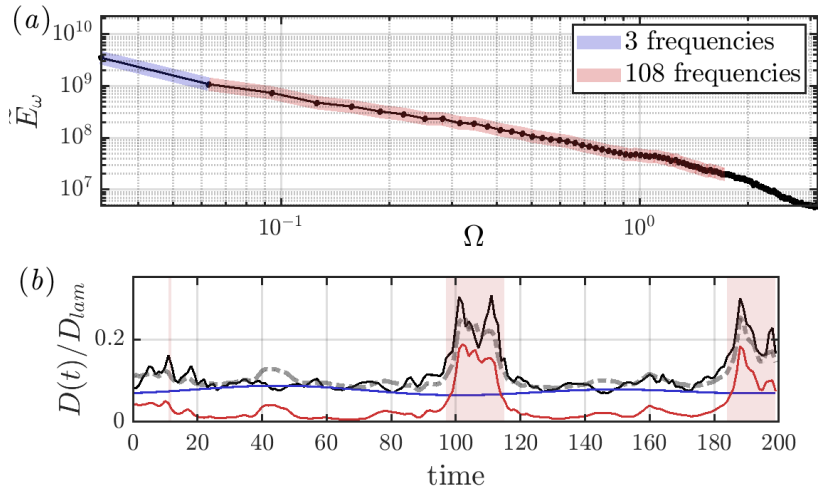


Figure 2: (a) The ensemble-averaged Fourier spectrum is shown in black, and the frequencies used to reconstruct the quiet region and the burst event, separately, are shaded in blue and red, respectively. (b) The full data (for $k_x = 0, 1, 2, 3$) (black) is compared to the reconstructions of the quiet region (blue) and the burst event (red) using the shaded frequencies in (a). For comparison, the grey dashed-dot line shows the sum of the blue and the red lines.

of vorticity $\omega(x, y, t)$ spaced apart by time dt . Each of the N_e realisations are therefore $T = N_t dt$ long. Here, to obtain one such realisation of the burst event, the start of a burst event T_b is first identified using the condition $D(t)/D_{lam} > 0.15$. The realisation of the burst event is then taken to be $T_b - 100 \leq t \leq T_b + 100$. (The reasons for choosing such time-windows, instead of the more generally used consecutive time-blocks, will become apparent when considering the wavelet spectrum in figure 4 of the next section.) For the DNS dataset considered here, we split the data to obtain $N_e = 50$ realisations of the burst event with each realisation having $N_t = 200$ and $dt = 1$, and therefore $T = 200$. It is ensured that no two realisations of the burst event have more than 50% overlap.

Let us now consider the Fourier transform of the vorticity $\omega(x, y, t)$ in time

$$\omega(x, y, t) = \sum_{\Omega=0}^{N_t-1} \tilde{\omega}(x, y; \Omega) e^{i(2\pi/T)\Omega t}, \quad (4.6)$$

where (\cdot) here represents the temporal Fourier transform. The corresponding Fourier spectrum is $\tilde{E}_\omega(\Omega) = \left[\int_0^{2\pi} \int_0^{2\pi} \tilde{\omega} \tilde{\omega}^* dx dy \right]_{N_e}$, with $(\cdot)^*$ representing complex conjugate.

Here $[\cdot]_{N_e}$ represents an averaging across the N_e different realisations of the burst event. Figure 2(a) shows the obtained Fourier spectrum. To isolate the quiet region and the burst events, we will use distinct sets of frequencies. The blue-shaded frequencies in figure 2(a) are used for the quiet region and the red shaded frequencies for the burst event. Let us denote the reconstruction of the data using this truncated Fourier basis as $\omega_r(x, y, t)$. Figure 2(b) shows the time-series of the reconstructions $\langle \omega_r, \omega_r \rangle_{x,y} / D_{lam}$ of the quiet region in blue and the burst event in red. These reconstructions are compared with the full data $\langle \omega, \omega \rangle_{x,y} / D_{lam}$ in black.

The number of modes required for isolating the different regions is identified by defining an error $\epsilon(t)$ in the projection of $\omega_r(x, y, t)$ onto $\omega(x, y, t)$, where $\epsilon(t) :=$

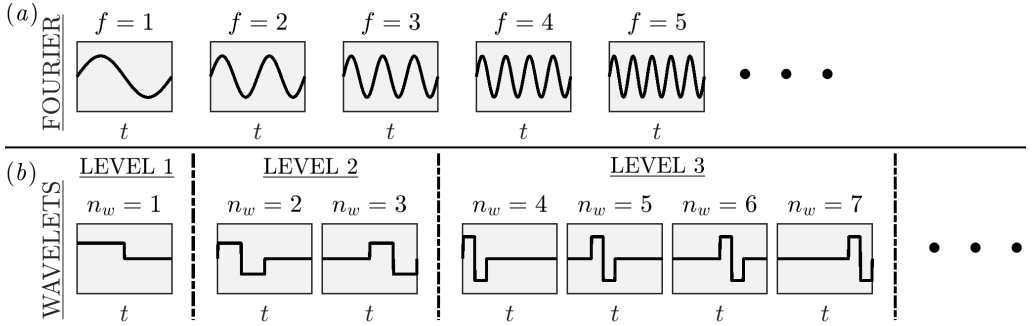


Figure 3: Schematic showing (a) the Fourier basis and (b) the discrete wavelet basis of Daubechies 1. The vertical dashed-dot lines in (b) demarcate the different levels of the wavelet basis, and will be used again in figure 5(a) when plotting the wavelet spectrum.

$1 - \langle \omega_r, \omega \rangle_{x,y} / \langle \omega, \omega \rangle_{x,y}$. Let $[\cdot]_t$ denote averaging in time. The blue-shaded frequencies in figure 2(a) ensure that $[\epsilon(t_q)]_t < 0.2$ where t_q is defined as the times t when $D(t)/D_{lam} \leq 0.1$, i.e. the quiet region. Similarly, the red-shaded frequencies in figure 2(a) ensure that $[\epsilon(t_b)]_t < 0.4$ where t_b is defined as the times t when $D(t)/D_{lam} \geq 0.15$, i.e. the bursting event. The numerical values of $[\epsilon(t_q)]_t < 0.2$ and $[\epsilon(t_b)]_t < 0.4$ simply ensure that the dominant frequencies (or wavelets as in the next section) are included, and changing the values does not significantly impact any of the discussions in this work.

From figure 2(b), we find that the Fourier basis is not able to efficiently isolate the burst event, because the red line does not go to zero in the quiet regions of the flow. Additionally, we require a significant number of frequencies to reconstruct the burst event. This is expected since we are trying to represent a localized event using the Fourier basis that is global. In order to remedy these problems, in the next section we will explore using a localized basis – wavelets – for this purpose.

5. Decomposing the flow: Wavelet bases

We now employ a wavelet basis to capture the burst events. The discrete Daubechies 1 (DB1) wavelets will be used for a majority of this work. The only exception is Appendix B, where for a different choice of wavelets, that of Daubechies 2, we will see that the discussions in this work remain similar.

5.1. Daubechies 1 wavelet basis and wavelet transform

To obtain a wavelet basis $\Theta_{n_w}(t)$, we first make a choice of the wavelet corresponding to $n_w = 1$, i.e. $\Theta_1(t)$, which is the mother wavelet. For the Daubechies 1 wavelet basis used in this work, the mother wavelet is a step function as shown in the first panel of figure 3(b). The mother wavelet covers the entire time domain and is said to belong to the lowest level, level 1, of the wavelet basis. To get level 2 of this wavelet basis, the mother wavelet is compressed by half. Now we need two wavelets to cover the entire domain, and these are shown as $n_w = 2$ and $n_w = 3$ in figure 3(b). Level 3 comprises of the mother wavelet compressed by a factor of four, and then repeated four times to cover the domain. This level is as shown by $n_w = 4-7$ in figure 3(b). The vertical black dashed-dot lines in figure 3(b) demarcate the different levels of the wavelet transform. Throughout this manuscript, we will use such vertical black dashed-dot lines to demarcate the levels. We see that, when considering wavelets, there are two factors that are important: (i) the compression of the wavelet, which is related to the concept of frequency in the Fourier

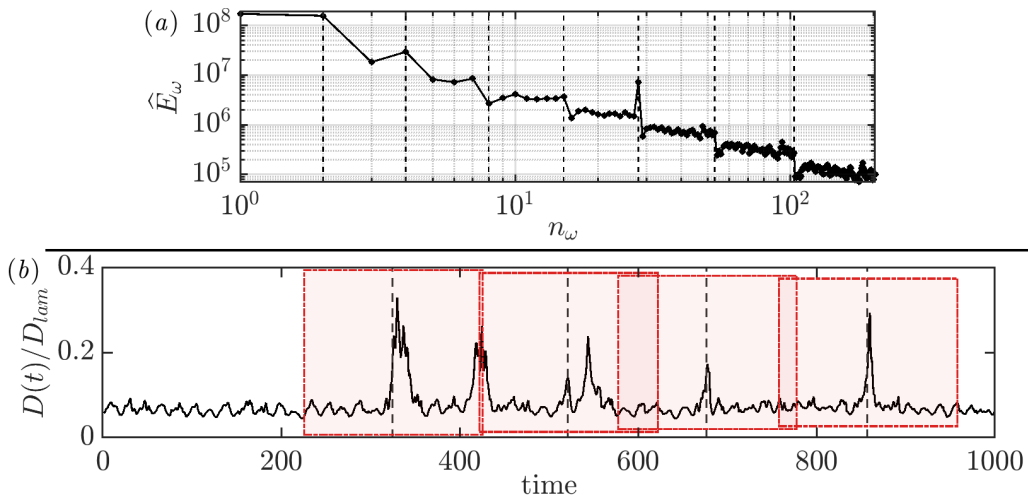


Figure 4: (a) The ensemble-averaged wavelet spectrum is shown for the case when ensembles are chosen as consecutive time-blocks. (b) A different strategy for choosing ensembles is also illustrated where the window is chosen such that a burst lies at the centre of it.

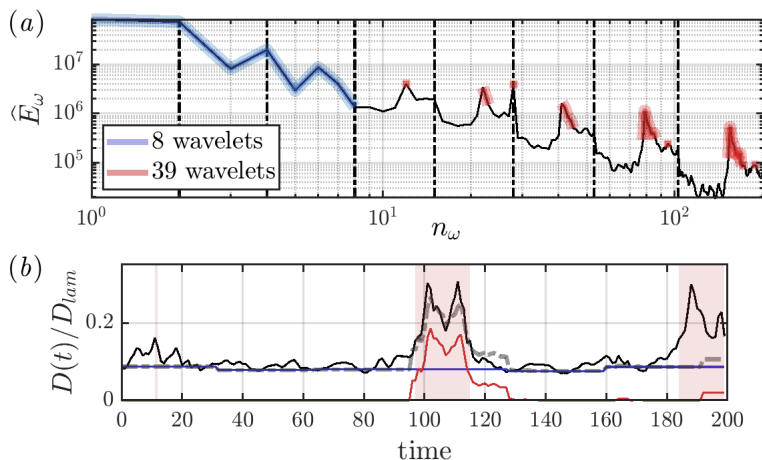


Figure 5: (a) The ensemble-averaged wavelet spectrum is shown in black, and the wavelets used to reconstruct the separate regions in (b) are shaded in different colours: the 8 wavelets for the quiet region are shaded in blue and the 39 wavelets for the burst event are in red. The vertical dashed lines indicate the different levels of the wavelet spectrum (see figure 3). (b) The full data for $k_x = 0, 1, 2, 3$ (black) is compared to the reconstructions (using the shaded frequencies in (a)) of the quiet region (blue) and the burst event (red). For comparison, the grey dashed-dot line shows the sum of the blue and the red lines.

domain and (ii) the location of the wavelet in time, which has no equivalent in the Fourier basis.

Similar to the Fourier transform in §4, we obtain a wavelet transform of $\omega(x, y, t)$ as

$$\omega(x, y, t) = \sum_{n_w=0}^{N_w} \hat{\omega}(x, y; n_w) \Theta_{n_w}(t), \quad (5.7)$$

where $(\hat{\cdot})$ represents the wavelet transform. The wavelet spectrum can then be obtained as $\hat{E}_\omega(n_\omega) = \left[\int_0^{2\pi} \int_0^{2\pi} \hat{\omega} \hat{\omega}^* dx dy \right]_{N_e}$.

5.2. Burst centred windowing

Before looking at the wavelet spectrum, let us briefly discuss the choice of the N_e realisations of the burst event. Generally, to obtain the different ensembles for ensemble averaging, we split the available data into several consecutive data-blocks of equal length, and compute the spectrum for each of these ensembles. The spectra are then averaged across the ensembles. The wavelet spectrum obtained from such consecutive ensembles is shown in figure 4(a). Within each of the levels (indicated by the vertical dashed-dot lines), we see that there are no noticeable trends, and peaks are notably absent. This absence of peaks can be explained by recalling that the location in time is important when considering wavelets. In this case, for each ensemble, the burst events occur at different locations in time and therefore appear at different n_w .

To remedy this, we will adopt the alternative windowing strategy that was briefly mentioned in §4 and depicted in figure 4(b). A realisation of the burst event is defined using the start of a burst event T_b as $T_b - 100 \leq t \leq T_b + 100$, where T_b is identified using the condition $D(t)/D_{lam} > 0.15$. As in §4, here we will consider $N_e = 50$ realisations of the burst event, each containing $N_t = 200$ time-snapshots of vorticity $\omega(x, y, t)$ spaced apart by time $dt = 1$. The spectrum obtained from this new windowing strategy is shown in figure 5(a). From the the red shaded regions of the spectrum in figure 5(a), we observe clear peaks in the lower levels that are present because of the burst events. In the next section we will more clearly show that these peaks correspond to the burst events.

5.3. Wavelet spectrum and wavelet-based flow reconstructions

The number of levels present in the spectrum is determined by the length of the time window (here $T = 200$) and the type of wavelet used (here DB1). In figure 5(a) there are 8 levels that are demarcated by the vertical dashed-dot lines. We will use distinct sets of wavelets to isolate the quiet region and the burst events. The first 3 levels will be used to reconstruct the quiet region, and these are shaded in blue. Next, 20% of the most energetic modes in levels 4-8 will be used to reconstruct the burst event, and these are shaded in red. As in §4, the number of wavelets used to reconstruct the flow is chosen such that the error $[\epsilon(t_q)]_t < 0.2$ and $[\epsilon(t_b)]_t < 0.4$ (see §4 for the definition of the error metric). Let us denote the data reconstructed using a truncated wavelet basis as $\omega_r(x, y, t)$. Figure 2(b) shows the time-series of the reconstructions $\langle \omega_r, \omega_r \rangle_{x,y} / D_{lam}$ of the quiet region in blue and the burst event in red. The reconstructions are compared with the full data $\langle \omega, \omega \rangle_{x,y} / D_{lam}$ in black. We observe that isolating the quiet region and the burst events is approximately possible using wavelets.

In comparing the wavelet-based reconstruction in figure 5(b) to the Fourier-based reconstruction in figure 2(b), three observations stand out. Firstly, and most importantly, wavelets are able to isolate the burst events better than the Fourier basis. To understand why, let us turn our attention to the relatively small magnitude (relative to the burst events) oscillations in the quiet region of the flow. When considering the Fourier basis, the same Fourier frequencies contribute both to these quiet oscillations as well as the burst events. However, since these oscillations occur at different locations in time relative to the burst events, the wavelet basis is able to produce reconstructions of the burst event uncontaminated by the quiet oscillations. Secondly, to reconstruct the burst event, fewer wavelets are required in comparison to Fourier frequencies: 39 wavelets as opposed to 108 (54 positive) Fourier frequencies. Finally, from figure 2(b) we see that wavelets are able

to isolate a single burst event, in contrast to the Fourier-based reconstruction in figure 2(b) where both the burst events are captured equally. Therefore, isolating single burst events, when there are multiple similar events present in a time window, is only possible using the wavelets bases.

We can therefore conclude that wavelets are better at isolating the burst events. Using wavelets we are able to obtain a signal of the burst event that is uncontaminated by the oscillations in the quiet region. Additionally, wavelets enable a lower-order representation of the burst event by requiring fewer wavelets (than Fourier frequencies) to reconstruct the burst event. In the next section we will therefore concentrate on using the wavelet basis to probe the flow patterns active in the quiet region and the burst events.

6. Coherent structures in intermittent flows: A Wavelet-POD analysis

The aim of both the current and the next section is to examine the coherent structures in an intermittent flow. A coherent structure is here defined as a flow pattern that maintains a significant degree of correlation with itself over a range of space and time (Robinson 1991). In this work, we are particularly interested in coherent structures identified using POD-based techniques. POD, introduced by Lumley (1967, 1970), is a commonly employed technique to find the flow patterns that are energetically dominant.

Many adaptations of POD, tailored for various classes of problems, are found in the literature (for instance, see reviews by Taira *et al.* (2017) and Rowley & Dawson (2017) and references therein). We are here interested in finding structures that are coherent in space and time, and a recently introduced POD-based technique for this purpose is spectral-proper-orthogonal-decomposition (SPOD) (Towne *et al.* 2018). In this method, the flow is first projected onto a Fourier basis. Thereafter, a proper orthogonal decomposition (POD) is performed at each Fourier frequency that gives coherent structures at that particular frequency. These structures are coherent in space due to the properties of POD and coherent in time since they are Fourier modes. However, in §5, we saw that a wavelet basis is better at characterising intermittent flows. Therefore, instead of a SPOD, here we will use a wavelet-proper orthogonal decomposition (WPOD). Using this method we will obtain structures that are coherent in space, and both coherent as well as localised in time since they are wavelet coefficients.

Before describing WPOD, to provide context, let us briefly consider the regular POD. In this case, we have velocity fields $\mathbf{q}(x, y, t) = (u(x, y, t), v(x, y, t))$ for a range of time. The POD modes $\phi_i(x, y)$ give an orthogonal basis for $\mathbf{q}(x, y, t)$, such that the 1st POD mode captures the largest variance of the data, the i^{th} POD mode captures the i^{th} largest variance, and so on. In other words, if \mathcal{E}_i is the projection of the data $\mathbf{q}(x, y, t)$ onto the i^{th} POD mode $\phi_i(x, y)$

$$\mathcal{E}_i = \frac{\left[|\langle \mathbf{q}(x, y, t), \phi_i(x, y) \rangle_{x,y} |^2 \right]_t}{\langle \phi_i(x, y), \phi_i(x, y) \rangle_{x,y}}, \quad (6.8)$$

then $\mathcal{E}_i > \mathcal{E}_{i+1}$. Here, as before, $[\cdot]_t$ denotes averaging in time, $\langle a, b \rangle_{x,y}$ denotes the inner product $\int_0^{L_y} \int_0^{L_x} b^*(x, y, t) a(x, y, t) dx dy$, and $|\cdot|$ represents absolute value. The problem of finding POD modes reduces to finding the eigenvalues of the correlation matrix QQ^* where Q is a matrix with columns containing $\mathbf{q}(x, y, t)$, i.e. the 1st column of Q is $\mathbf{q}(x, y, t_1)$ and the i^{th} column is $\mathbf{q}(x, y, t_i)$. The eigenvectors of QQ^* are equivalently the left singular vectors of the matrix Q , and therefore the problem can be solved by performing a singular value decomposition of the data-matrix Q .

Rather than finding the coherent structures in the entire flow using POD, we are

interested in finding the coherent structures at particular wavelets. Let us therefore consider wavelet-POD. For this, first consider the N_e different realisations of the burst event (see §5 for how each realisation is chosen from the data). From these N_e realisations, consider one realisation n_e , where now $1 \leq n_e \leq N_e$. At this n_e we have the data $\mathbf{q}(x, y, t; n_e) = (u(x, y, t; n_e), v(x, y, t; n_e))$. A wavelet transform of this n_e^{th} realisation of the burst event will give us $\hat{\mathbf{q}}(x, y; n_w, n_e) = (\hat{u}(x, y; n_w, n_e), \hat{v}(x, y; n_w, n_e))$, where \hat{u} and \hat{v} represents the wavelet transform of u and v . Therefore, for each wavelet n_w , and from each realisation of the burst event n_e , we have the state vector $\hat{\mathbf{q}}(x, y; n_w, n_e)$. If we now concentrate on just one wavelet n_w , we have N_e data vectors $\hat{\mathbf{q}}(x, y; n_w, 1 : N_e)$.

The objective now is to find basis vectors $\hat{\phi}_i(x, y; n_w)$ such that

$$\hat{\mathbf{q}}(x, y; n_w, n_e) = \sum_{i=0}^{N_e} a_i(n_w, n_e) \hat{\phi}_i(x, y; n_w). \quad (6.9)$$

For each n_w , the equivalent of the POD energy in (6.8) now becomes

$$\hat{\mathcal{E}}_i(n_w) = \frac{\left[\left| \langle \hat{\mathbf{q}}(x, y; n_w, n_e), \hat{\phi}_i(x, y; n_w) \rangle_{x,y} \right|^2 \right]_{n_e}}{\langle \hat{\phi}_i(x, y; n_w), \hat{\phi}_i(x, y; n_w) \rangle_{x,y}}, \quad (6.10)$$

where $\hat{\mathcal{E}}_i(n_w) \geq \hat{\mathcal{E}}_{i+1}(n_w)$. It should be noted that, unlike in (6.8) where the averaging is over time, in (6.10) the averaging is across the N_e different realisations of the burst event (denoted by $[\cdot]_{n_e}$). If we consider the WPOD modes across all n_w and pick the dominant mode with energy $\mathcal{E}_1 = \max_{n_w}(\hat{\mathcal{E}}_1(n_w))$, then the projection that is maximised is

$$\mathcal{E}_1 = \frac{\left[\left| \langle \mathbf{q}(x, y, t; n_e), \phi_1(x, y, t) \rangle_{x,y,t} \right|^2 \right]_{n_e}}{\langle \phi_1(x, y, t), \phi_1(x, y, t) \rangle_{x,y,t}}, \quad (6.11)$$

where $\langle a, b \rangle_{x,y,t}$ denotes the inner product $\int_0^T \int_0^{L_y} \int_0^{L_x} b^*(x, y, t) a(x, y, t) dx dy dt$. Here $\phi_i(x, y, t)$ represents the WPOD mode $\hat{\phi}_i(x, y; n_w)$ in time, i.e. $\phi_i(x, y, t)$ is an inverse wavelet transform of $\hat{\phi}_i(x, y; n_w)$.

In practice, to do a WPOD and find $\hat{\mathcal{E}}_i(n_w)$ and $\hat{\phi}_i(x, y; n_w)$, we solve for the eigenvalues of the correlation matrix $\hat{Q}_{n_w} \hat{Q}_{n_w}^*$ where the columns of \hat{Q}_{n_w} are the data $\hat{\mathbf{q}}(x, y; n_w, 1 : N_e)$, such that the 1st column corresponds to $\hat{\mathbf{q}}(x, y; n_w, 1)$, the i^{th} column to $\hat{\mathbf{q}}(x, y; n_w, i)$, and so on. The eigenvalues of $\hat{Q}_{n_w} \hat{Q}_{n_w}^*$ can also be obtained from a singular value decomposition of \hat{Q}_{n_w} . The i^{th} left singular vector is the i^{th} WPOD mode and the square of the i^{th} singular value is the corresponding WPOD energy $\hat{\mathcal{E}}_i(n_w)$ (6.10).

6.1. WPOD spectrum and modes for the Kolmogorov flow

Figure 6(a) shows the WPOD energies $\hat{\mathcal{E}}_i(n_w)$ (6.10) as a function of wavelet n_w . The darkest line represents the 1st WPOD mode ($\hat{\mathcal{E}}_1(n_w)$) and lighter colours represent the higher modes. The first 10 modes are shown here. Both the x and y axes in figure 6(a) are shown in logarithmic scale. The black vertical dashed-dot lines demarcates the different levels of the wavelet transform (see §5.1). The shaded boxes represent the subset of wavelets that are responsible for the quiet regions in blue and the burst event in red (see §5). Figures 6(b-f) shows the first 5 WPOD modes for $n_w = 2$ corresponding to the blue line in figure 6(a), i.e. a n_w corresponding to the quiet region. Similarly, figures 6(g-k) shows the first 5 WPOD modes for $n_w = 22$ corresponding to the red line in figure 6(a), i.e. a n_w corresponding to the burst event.

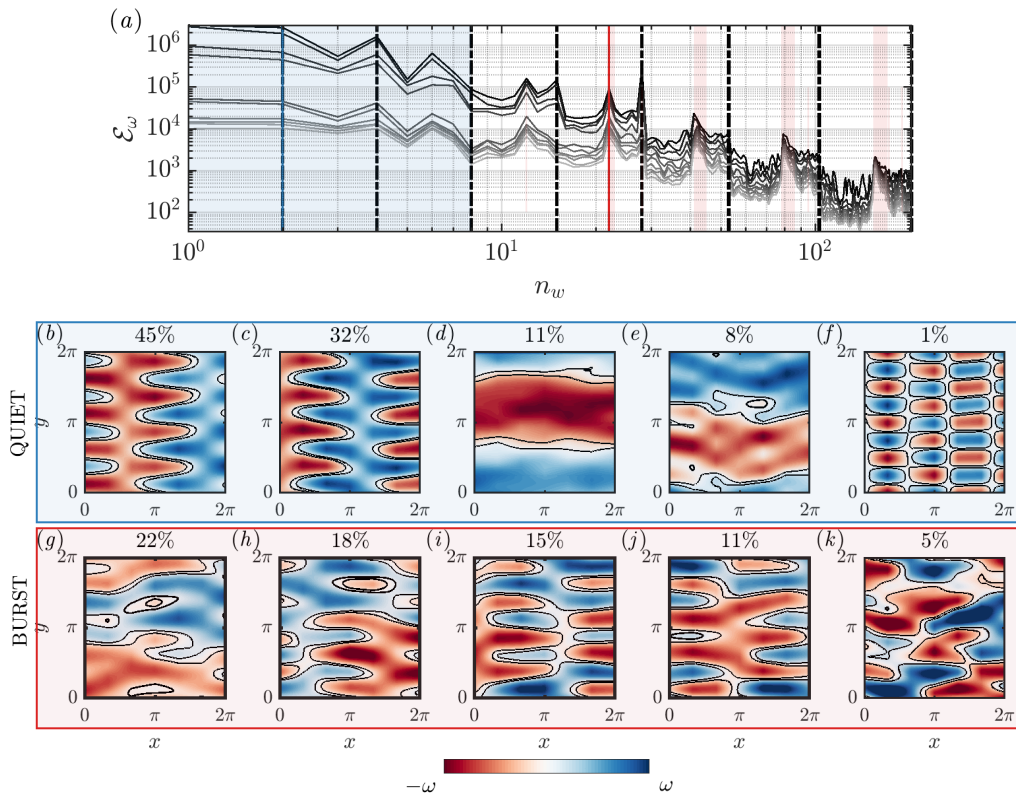


Figure 6: (a) The WPOD spectrum is shown as a function of wavelet n_w . The energies of the first 10 WPOD modes are shown with the lighter lines representing the higher modes. The vertical dashed-dot lines demarcate the levels of the wavelet transform. The shaded regions represent the wavelets that are responsible for the quiet region in blue and the burst event in red. The first 5 WPOD modes are shown for two different wavelets n_w : (b-f) $n_w = 2$ responsible for the quiet region (b marked by the blue vertical line in (a)) and (g-k) $n_w = 22$ responsible for the burst event (k marked by the red vertical line in (a)).

Let us consider the WPOD spectrum in figure 6(a), and first focus on the wavelets responsible for the quiet region shaded in blue, i.e. the first two levels of the wavelet transform. Notably, only the lower levels show any appreciable low-rank behaviour, i.e. within these levels the first few WPOD modes capture significantly more energy than the higher modes. Low-rankness in the WPOD spectrum suggests that there is an energetically dominant mechanisms that is responsible for the quiet region of the flow. To probe this further, let us now look at the WPOD modes at $n_w = 2$ in figures 6(b-f). The WPOD modes 1 and 2, as well as modes 3 and 4, are shifted versions of the same mode, a result of the inherent symmetries in the flow. (While symmetries can be incorporated into the POD modes, the instantaneous fluctuations of the flow do not adhere to these symmetries and so we present modes without symmetrization). Together, modes 1 and 2 account for 77% of the energy at this n_w . Crucially, these first two modes closely resemble the unstable eigenfunction obtained from the Navier-Stokes equations linearized around the mean flow (see appendix A). This indicates that this unstable eigenfunction is mainly responsible for the quiet region of this flow. This is consistent with the observations in

Farazmand & Sapsis (2017), where they employed an alternative strategy to capture this unstable eigenfunction, and used it to predict the burst events. Moving on to modes 3 and 4, while these modes are energetically significant, they captures less energy compared to modes 1 and 2. Together they capture 19% of the energy at this n_w . Structurally, modes 3 and 4 capture shearing motions.

Let us now turn our attention to the the wavelets responsible for the burst event. These wavelets are shaded in red in figure 6(a). One initial observation is that there is no significant low-rankness at a majority of these wavelets. This lack of low-rankness generally suggests that there is no one dominant mechanism that is responsible for the burst event. To investigate these modes further, consider the WPOD modes at $n_w = 22$ in figures 6(g-k). Notably, the first 4 WPOD modes in the burst event are structurally similar to the modes in the quiet region. Additionally, we observe that modes 2-4, while being similar to the unstable eigenfunction, are fragmented versions of this eigenfunction.

From these observations, we can hypothesise that the shearing motions are responsible for disrupting the flow due to the unstable eigenfunction, and intermittently, this shearing disrupts the mode enough to cause a burst event. While a WPOD analysis can suggest that such a mechanism causes the burst events, to conclusively show this we need to do a dynamic mode decomposition (Schmid 2022) analysis that identifies the relevant instabilities of the flow generated by the unstable eigenfunction. However, this falls beyond the scope of the current manuscript.

7. Coherent Structures in Quiet and Burst Regions - A Composite-WPOD Analysis

In this section we will introduce composite-WPOD. Instead of identifying structures at specific wavelets n_w as for WPOD in the previous section, in composite-WPOD we will identify the coherent structures for a band of wavelets (n_{w1}, n_{w2}, \dots) . This is important since, from §5 we know that, rather than individual wavelets, bands of wavelets contribute to the quiet region and the burst events. For example, to find modes for the quiet region, we need modes that represent the band of wavelets $\mathbf{n}^q = (n_{w1}^q, n_{w2}^q, \dots, n_{wN_q}^q)$ that are responsible for the quiet region (blue shaded values of n_w in figure 6(a)). We will therefore use a composite version of the WPOD used in §6.

In §6, to obtain the WPOD modes, we computed the SVD of a data matrix \hat{Q}_{n_w} . The columns of \hat{Q}_{n_w} were taken to be the data $\hat{\mathbf{q}}(x, y; n_w, 1 : N_e)$, such that the 1st column corresponds to $\hat{\mathbf{q}}(x, y; n_w, 1)$, the i^{th} column to $\hat{\mathbf{q}}(x, y; n_w, i)$, and so on. Here we will instead consider the data matrix \hat{P} that contains coefficients at all the n_w that is contained in \mathbf{n}^q such that:

$$\hat{P} = [\hat{\mathbf{q}}(x, y; n_{w1}^q, 1), \dots, \hat{\mathbf{q}}(x, y; n_{w1}^q, N_e), \dots, \hat{\mathbf{q}}(x, y; n_{wi}^q, 1), \dots, \hat{\mathbf{q}}(x, y; n_{wi}^q, N_e), \dots]. \quad (7.12)$$

In effect, to obtain \hat{P} , we horizontally stack all the N_q number of \hat{Q}_{n_w} that correspond to the n_w in \mathbf{n}^q , i.e. $\hat{P} = [\hat{Q}_{n_{w1}^q}, \hat{Q}_{n_{w2}^q}, \dots, \hat{Q}_{n_{wi}^q}, \dots]$. The SVD of \hat{P} will give us the dominant structures that are responsible for the collection of wavelets \mathbf{n}^q .

We will denote the composite-WPOD energies for wavelets \mathbf{n}^q , obtained as the square of the singular values of \hat{P} , as $\tilde{\mathcal{E}}_i^q$. In other words, $\tilde{\mathcal{E}}_1^q$ is the energy of the dominant composite-WPOD mode that captures the dynamics across the set of wavelets \mathbf{n}^q . The first 5 such composite-WPOD modes for the set of wavelets \mathbf{n}^q are shown in figures 7(b-f). The titles of these plots shows the percentage energy captured by the mode, i.e. $100 \times \tilde{\mathcal{E}}_i^q / (\sum_{j=0}^{M_q} \tilde{\mathcal{E}}_j^q)$. Similarly, composite-WPOD modes can be obtained for the wavelets

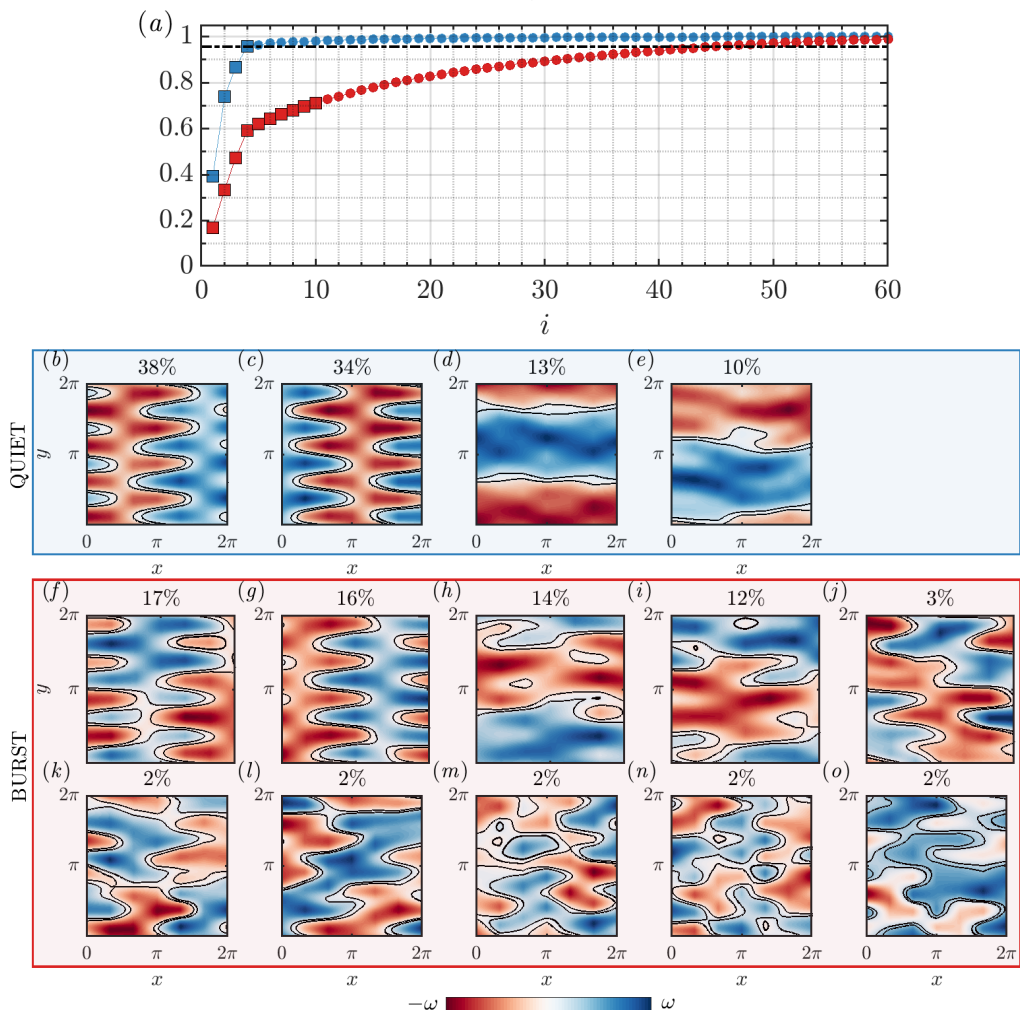


Figure 7: The first 5 composite-WPOD modes are shown for two different wavelets bands: (b-e) wavelets responsible for the quiet region marked by the blue shaded region in figure 6(a) and (f-o) wavelets responsible for the burst event marked by the red shaded regions in figure 6(a). (a) Also shown is the cumulative contribution of the first i modes to the total energy for the quiet regions (blue line) and the burst events (red line).

\mathbf{n}^b that contribute to the burst events, and here we denote the WPOD energies of these modes as $\tilde{\mathcal{E}}_j^b$. The first 10 among these WPOD modes for the burst event are shown in figures 7(f-o). Figure 7(a) shows the cumulative contribution of the first i modes to the total energy. In other words, the blue line in figure 7(a) shows $(\sum_{j=0}^i \tilde{\mathcal{E}}_j^q) / (\sum_{j=0}^{M_q} \tilde{\mathcal{E}}_j^q)$, where $M_q = N_e \times N_q$ is the total number of composite-WPOD modes obtained for the set of wavelets \mathbf{n}^q for the quiet region. The red line shows the same quantity for the $M_b = N_e \times N_b$ composite-WPOD modes corresponding to the set of wavelets \mathbf{n}^b for the burst event. In this study $N_e = 50$, $N_q = 8$ and $N_b = 39$ (see figure 5 (a)), and therefore $M_q = 400$ and $M_b = 1950$. The horizontal dashed-dot line in figure 7(a) indicates 95%.

Let us first focus on the quiet region. From the blue line in figure 7(a) we see that the curve very quickly approaches the dashed-dot line indicating 95%. The first four modes

(square markers) capture most of the energy of the flow. These four modes are shown in figures 7(b-e), and they can be compared to their counterparts in figures 6(b-e). We note that the leading modes obtained from both WPOD versions are similar. Consistent with the observations from figures 6, composite-WPOD modes 1 and 2 correspond to the unstable eigenfunction and modes 3 and 4 represent shearing motions. (The modes in figure 7 exhibit greater convergence compared to those in figure 6 due to the inclusion of data from a collection of n_w , thereby increasing the input data used.)

Now consider the burst region. From the red line in figure 7(a), we see that the increase in total energy is more gradual. The first four modes, shown in figures 7(f-i), still capture a considerable part of the energy. Structurally, these four modes resemble the modes in the quiet region. This is consistent with the observation in §6, and shows that the dominant modes in the quiet region persist during the burst events as well. In effect, this flow cannot be precisely divided into the quiet region and the burst events. However, going back to figure 7(a), the red line shows a very slow increase, and a large number of sub-optimal modes are required to reach 95% energy (the horizontal dashed-dot line). Therefore, although these sub-optimal modes (i.e. mode 5 and onward) each contribute very little energy, large numbers of them together play a significant role in the burst events. A few of these modes are shown in figures 7(j-o). The leading among these modes appear to be modified, here sheared, versions of the unstable eigenfunction (see for example figures 7(j), 7(k) and 7(l)). This is also consistent with the observations in §6.1. Notably, such fragmented and sheared versions of the unstable eigenfunction are modes that are typical to the burst events.

7.1. Tracking composite-WPOD modes

So far we have identified coherent structures that exist in the quiet region and the burst events. In this section we will track these coherent structures in a time-series obtained from the flow. In other words, we are interested in analysing how the contributions of these coherent structures to the flow evolve with time. This will pave the way for the discussion in the next section (§8), where we will use these coherent structures to introduce the WPOD-based method 2 for predicting the burst events.

We have two sets of composite-WPOD modes: (i) let L_q represent the set of $M_q = N_e \times N_q$ number of composite-WPOD modes corresponding to the quiet region with the i^{th} mode in L_q having WPOD energy $\tilde{\mathcal{E}}_i^q$ and similarly (ii) let L_b represent the set of $M_b = N_e \times N_b$ modes for the burst event with energies $\tilde{\mathcal{E}}_i^b$. Consider the modes $\phi_j^q(x, y)$ ($j = 1, \dots, M_q$) from L_q . Now consider a time series $\mathbf{q}(x, y, t)$ obtained from flow, where $\mathbf{q} = (u, v)$ is the state vector. Note that $\mathbf{q}(x, y, t)$ can be a time-series of arbitrary length with any number of burst events occurring at any point in time. Additionally, $\mathbf{q}(x, y, t)$ could lie outside the time-window used to obtain the N_e realisations of the burst event for WPOD (as required for the problem of predicting the burst events in the next section). At each time t , we aim to assess the presence of the structures $\phi_j^q(x, y)$ in the flow field $\mathbf{q}(x, y, t)$. For this, we will first compute $E_{qj}(t)$, which is the magnitude of energy shared between a mode $\phi_j^q(x, y)$ and $\mathbf{q}(x, y, t)$ as:

$$E_{qj}(t) := \int_{k_y} \int_{k_x} \left| \tilde{q}(k_x, k_y; t) \tilde{\phi}_j^q(k_x, k_y; t)^* \right|^2 dk_x dk_y. \quad (7.13)$$

Here $\tilde{\cdot}$ represents the 2D Fourier transform in the spatial directions, and k_x and k_y are the wavenumbers in the x and y -directions, respectively. We will normalise $E_{qj}(t)$ using (i) $E_{jj} := \langle \phi_j^q, \phi_j^q \rangle_{x,y}$ which is the energy of $\phi_j^q(x, y)$ and (ii) $E_{qq}(t) := \langle \mathbf{q}, \mathbf{q} \rangle_{x,y}$ which is the energy of $\mathbf{q}(x, y, t)$.

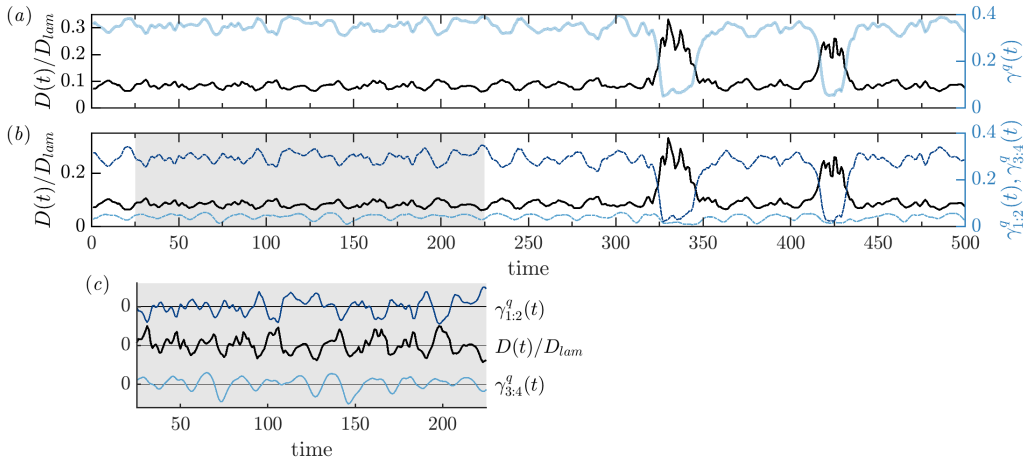


Figure 8: (a) Tracking coherent structures for the quiet region using γ^q (blue line). (b) Two components of γ^q are also shown: $\gamma_{1:2}^q(t)$ in darker blue and $\gamma_{3:4}^q(t)$ in lighter blue. (c) Also shown are the mean-removed and normalised profiles of $D(t)/D_{lam}$, $\gamma_{1:2}^q(t)$ and $\gamma_{3:4}^q(t)$ for the time-window indicated by the grey-shaded box in (b).

The coherence $\gamma^q(t)$ between $\mathbf{q}(x, y, t)$ and the modes in L_q can now be defined as:

$$\gamma_j^q(t) = \frac{E_{qj}(t)}{E_{qq}(t) E_{jj}}, \quad \gamma^q(t) = \frac{1}{M_q} \sum_{j=1}^{M_q} \left(\frac{\tilde{\mathcal{E}}_i^q}{\sum_{j=0}^{M_q} \tilde{\mathcal{E}}_j^q} \right) \gamma_j^q(t). \quad (7.14)$$

Here $\gamma_j^q(t)$ is the coherence between a point in the time-series from the flow $\mathbf{q}(x, y, t)$ and the j^{th} composite-WPOD mode in L_q . Hence $\gamma^q(t)$ is the weighted average of the coherence across the M_q different modes in L_q , weighted by the fraction of energy that each mode contributes to the energy of the quiet region. Similarly, we can also define $\gamma^b(t)$ as the average coherence of $\mathbf{q}(x, y, t)$ with structures in L_b . It should be noted that, the actual value of $\gamma^q(t)$ and $\gamma^b(t)$ do not hold physical significance, as these quantities are obtained as energy-weighted means of several modes, many of which contribute minimally to the overall energy. Instead, our interest is in the trends of $\gamma^q(t)$ and $\gamma^b(t)$ over time.

Let us first consider $\gamma^q(t)$ for a sample time-series. Figure 8(a) displays $\gamma^q(t)$ in blue, along with the time-series of enstrophy $\langle \omega, \omega \rangle_{x,y} / D_{lam}$ in black. To obtain a smoother curve, the average of $\gamma^q(t-2)$, $\gamma^q(t-1)$ and $\gamma^q(t)$ is computed at each time t . Similar averaging is also later carried out for $\gamma^b(t)$. (It is important to note that, at each time t_1 , only values $t \leq t_1$ are used for this averaging). From figure 8(a) we observe that: (i) within the quiet region, $\gamma^q(t)$ remains relatively high and (ii) $\gamma^q(t)$ plummets down when burst events occur. It is evident that $\gamma^q(t)$ exhibits distinctive changes in its trends during a burst event. Looking ahead to the problem of predicting the burst events, $\gamma^q(t)$ should, therefore, become a valuable tool.

To further probe this, figure 8(b) shows two components of $\gamma^q(t)$: (i) $\gamma_{1:2}^q(t)$ in darker blue, which shows the weighted average of the coherence of just the first two modes in L_q , i.e. the unstable eigenfunction (modes in figures 7(b, c)) and (ii) $\gamma_{3:4}^q(t)$ in lighter blue, which is the weighted average coherence of modes 3 and 4, i.e. the shearing motions. (modes in figures 7(d, e)). The first significant observation is that $\gamma_{1:2}^q(t)$ closely follows the trends of $\gamma^q(t)$. This is not surprising given that, together, modes 1 and 2 capture more than 70% of the energy of the quiet region (as seen in figure 7). Therefore we can say that the trends of $\gamma^q(t)$ is most significantly impacted by the flow due to modes 1

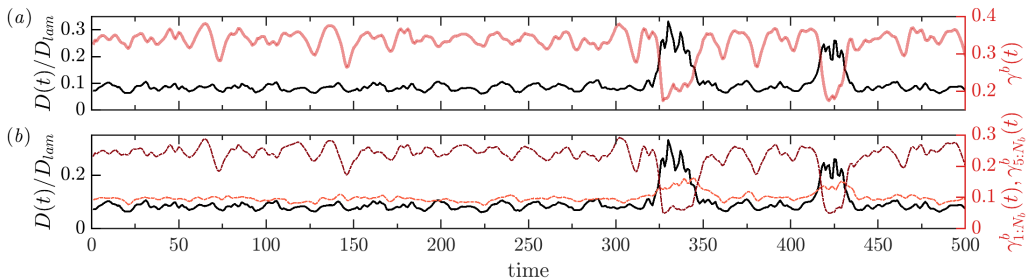


Figure 9: (a) Tracking coherent structures for the burst events using γ^b (red line). (b) Two components of γ^b are also shown: $\gamma^b_{1:4}(t)$ in darker red and $\gamma^b_{5:N_b}(t)$ in lighter red.

and 2, i.e. the unstable eigenfunction. The second noteworthy observation is that $\gamma^q_{3:4}(t)$ tends to move out of phase with $\gamma^q_{1:2}(t)$. This becomes more evident in figure 8(c) where mean-removed and normalised profiles of $\langle\omega, \omega\rangle_{x,y}$, $\gamma^q_{1:2}(t)$ and $\gamma^q_{3:4}(t)$ are shown. The curves are vertically shifted in order to make the trends clearer. From this figure we see that, when the total dissipation rate ($\langle\omega, \omega\rangle_{x,y}$) increases, the presence of the flow due to the unstable eigenfunction ($\gamma^q_{1:2}(t)$) decreases and that of the shearing structure ($\gamma^q_{3:4}(t)$) increases. This observation provides additional support to our initial hypothesis that the shearing motions disrupt the flow generated by the unstable eigenfunction, thereby increasing the dissipation.

Let us now examine $\gamma^b(t)$ for the same time-series. Figure 9(a) shows $\gamma^b(t)$ in red alongside the time-series of enstrophy $\langle\omega, \omega\rangle_{x,y}/D_{lam}$ in black. Upon comparing $\gamma^b(t)$ with $\gamma^q(t)$ in figure 8(a), the first apparent observation is that the trends between them are strikingly similar. This observation is consistent with the earlier finding from figure 7, that nearly 60% of the energy of the burst events is captured by modes that are present in the quiet region. Looking ahead to the problem of predicting the burst events, this similarity between $\gamma^q(t)$ and $\gamma^b(t)$ brings the unfortunate conclusion that the trends of the full $\gamma^b(t)$ may not be useful for prediction. However, our earlier observations showed the existence of sub-optimal structures that are unique to the burst events (see figures 7). Presumably, these structures exhibit trends dissimilar to $\gamma^q(t)$. The question, therefore, is whether we can identify a component of $\gamma^b(t)$ that has predictive value?

To explore this further, in figure 8(b) $\gamma^b(t)$ is split into two components: (i) $\gamma^b_{1:4}(t)$ computed using just the first four modes in L_b , i.e. the modes that resemble those from the quiet region (modes in figures 7(f)-7(i)) and (ii) $\gamma^b_{5:N_b}(t)$ computed using modes 5 and onward (the first few of these modes were shown in figures 7(j)-7(o)). Two observations become immediately apparent. Firstly, as expected, $\gamma^b_{1:4}(t)$ follow trends similar to the full $\gamma^b(t)$ as well as $\gamma^q(t)$. Secondly, and also more interestingly, $\gamma^b_{5:N_b}(t)$ increases during the burst event. This again shows that these sub-optimal modes are unique to the burst events. Again looking ahead to the problem of predicting the burst events, these observations show that, although the full $\gamma^b(t)$ may not be helpful in identifying the burst events, the distinctive trends of $\gamma^b_{5:N_b}(t)$ during the burst event will be.

8. Predicting burst events using WPOD modes - Method 2

In this section, to predict the burst event, we will use the distinctive trends of $\gamma^q(t)$ and $\gamma^b_{5:N_b}(t)$ identified in the previous section. For this purpose, a predictor $\lambda = \gamma^q(t) - \gamma^b_{5:N_b}(t)$ is defined. Figure 10 shows $D(t)/D_{lam}$ along with the evolution of predictor λ for three different time-windows. The time-window in figure 10(a) was included among the $N_e = 50$

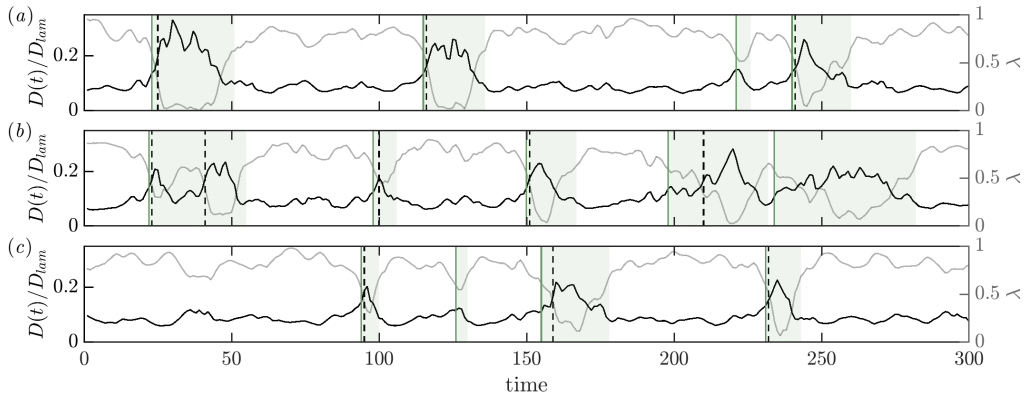


Figure 10: Predictions of the burst events obtained using the WPOD-based method 2 for three separate time-series from DNS. The green shaded regions indicate the identified burst regions where the predictor (grey line) has $\lambda < \lambda_t$. Vertical green lines mark the onset of these burst regions, representing the predictions of the burst event from the WPOD-based method. Predicted times are compared to those obtained from method 1 of tracking the energy of the flow (black dashed lines).

realisations of the burst events that was used for computing the WPOD modes, while the time-windows in figures 10(b) and 10(c) fall outside these N_e realisations. Since we are interested in the trends of λ , and not the magnitudes, we here consider normalised λ (normalised by the minimum and maximum values obtained within a time window $t = 0 - 15000$). From figure 10, we see that λ decreases during burst events. Consequently, we designate a threshold λ_t , and values of λ below λ_t will be identified as burst events.

To calculate λ_t , we begin by computing the mean of λ minus the variance, where both these statistics are calculated specifically for time instances that correspond to the quiet regions, i.e. where $D(t)/D_{lam} < 0.1$, between $t = 0 - 15000$. The threshold λ_t , as used in figure 16, is set to be 0.95 times this mean minus the variance. (The impact of varying this coefficient 0.95 to other values will be discussed in §10.1). The green shaded region marks the times where λ remains below λ_t , and the solid green vertical lines marks beginnings of these regions. Importantly, we notice that a majority of the green-shaded regions correspond to the burst events. The green vertical lines are therefore the predictions of the burst events obtained using this WPOD-based method. These predictions can be compared to those obtained using method 1 (i.e. times when $D(t)/D_{lam} \geq 0.15$) which are the black dashed vertical lines.

First, we note that the WPOD-based method is able to predict the burst events well. However, for most of the burst events in figure 10, the improvement in prediction times over the more straightforward method 1 is only marginal. Additionally, for this chosen threshold, we obtain false-positives, i.e. predictions of oncoming burst-events in the absence of such events (e.g. $t \approx 125$ in figure 10(c)). We can therefore conclude that the WPOD-based method is capable of predicting burst events with slightly improved prediction times compared to the more straightforward method of thresholding $D(t)/D_{lam}$, albeit with the possibility of some false-positives.

9. Forcing to the coherent structures

Up to this point, our focus has been on the coherent structures in the flow. We will now shift our attention to the forcing that generate these coherent structures. This

will thereafter pave the way for the discussion in the next section, where we will use the obtained forcing to introduce the WRA-based method 3 for predicting the burst events. To obtain this forcing, we will use resolvent analysis. Within the resolvent analysis framework, the non-linear terms of the linearized Navier–Stokes equations are considered to be a forcing to the linear equations (e.g. McKeon & Sharma 2010; Hwang & Cossu 2010; Moarref *et al.* 2013; Morra *et al.* 2021; Towne *et al.* 2020). Using this method, we obtain a complete basis that can be used to represent the flow. Additionally, it also gives us a forcing, i.e. the non-linear terms, that force the linearized equations to generate the observed coherent structures.

Conventionally, the resolvent analysis framework is established using a Fourier transform in time. However, here, for precise decomposition of the flow into the quiet and burst regions, we need to use a wavelet basis (see §5). Consequently, to obtain forcing structures for the quiet and the burst regions, we need to use wavelet-based resolvent operators. While a substantial amount of literature considers the Fourier-based resolvent analysis, studies that concentrate on the wavelet-based resolvent analysis (WRA) are limited and very recent (Ballouz *et al.* 2023*b,a*). The next section introduces the resolvent operator for a broader range of bases, which includes the Fourier and wavelet bases.

9.1. Resolvent operator

To define the resolvent operator, we will start with the linearized Navier–Stokes equations that was laid out in (3.4) and is reproduced here for the sake of clarity:

$$\dot{\tilde{\omega}}(y, t; k_x) + \mathbf{A}\tilde{\omega}(y, t; k_x) = \tilde{F}(y, t; k_x). \quad (9.15)$$

Here, a 1D Fourier transformation in the x -direction has already been carried out. Let us consider the basis vectors $\Theta_{n_w}(t)$. We can write $\tilde{\omega}$ in terms of its projection onto this basis as (Farge 1992):

$$\begin{aligned} \tilde{\omega}(y, t; k_x) &= \sum_{n_w=1}^{N_w} \hat{\omega}(y; k_x, n_w) \Theta_{n_w}(t), \quad \text{where} \\ \hat{\omega}(y; k_x, n_w) &= \int_0^T \tilde{\omega}(y, t; k_x) \Theta_{n_w}^*(t) dt. \end{aligned} \quad (9.16)$$

We can similarly obtain the wavelet coefficient $\hat{F}(y; k_x, n_w)$ of $\tilde{F}(y, t; k_x)$. Here T is the length of the time-window used. For the case considered here, T (here $T = 200$) is the length of a realisation of the burst event that we used for WPOD (see §5.2).

The basis $\Theta_{n_w}(t)$ is chosen such that it is complete. They are also orthogonal, i.e. $\int_0^T \Theta_{m_w}^* \Theta_{n_w} dt = \delta_{n_w m_w}$, where $\delta_{n_w m_w}$ is the Dirac delta function. The basis could, for instance, be the Fourier bases, where $\Theta_{n_w}(t) = \exp i(2\pi/T)n_w t$, or as will be considered here, the wavelet basis discussed in §5.1. The $\hat{\cdot}$ stands for the transform to the basis. For ease of notation, hereafter $\hat{\omega}(y; k_x, n_w)$ and $\hat{F}(y; k_x, n_w)$ will be denoted as $\hat{\omega}_{n_w}(y; k_x)$ and $\hat{F}_{n_w}(y; k_x)$, respectively. In terms of these transforms, the linearized equations in (9.15) become

$$\begin{aligned} \sum_{n_w=1}^{N_w} \hat{\omega}_{n_w}(y; k_x) \left(\frac{d\Theta_{n_w}(t)}{dt} \right) + \mathbf{A} \sum_{n_w=1}^{N_w} \hat{\omega}_{n_w}(y; k_x) \Theta_{n_w}(t) \\ = \sum_{n_w=1}^{N_w} \hat{F}_{n_w}(y; k_x) \Theta_{n_w}(t) \end{aligned} \quad (9.17)$$

Here N_w is the number of wavelet coefficients obtained from the wavelet transform (determined by the type of wavelet chosen and the number of time-instances N_t chosen for the time-window). The bases vectors $\Theta_{n_w}(t)$ are not guaranteed to be continuous or differentiable. For instance, the discrete Daubechies 1 wavelet that we will use (see §5.1) is discontinuous and not differentiable. To consider the formulation in terms of the most general bases, including discontinuous ones, we re-write (9.17) in terms of the integrals of the bases $\Theta_{n_w}(t)$, therefore giving us

$$\begin{aligned} \sum_{n_w=1}^{N_w} \widehat{\omega}_{n_w}(y; k_x) \Theta_{n_w}(t) + \mathbf{A} \sum_{n_w=1}^{N_w} \widehat{\omega}_{n_w}(y; k_x) \left(\int_0^t \Theta_{n_w}(t') dt' \right) \\ = \sum_{n_w=1}^{N_w} \widehat{F}_{n_w}(y; k_x) \left(\int_0^t \Theta_{n_w}(t') dt' \right). \end{aligned} \quad (9.18)$$

Since the bases are complete, the integral of a particular basis vector can be written as a linear superposition of all basis vectors, i.e. $\int_0^t \Theta_{n_w}(t') dt' = \sum_{m_w=1}^{N_w} c_{n_w m_w} \Theta_{m_w}(t)$, where $c_{n_w m_w}$ are scalar coefficients. This gives

$$\begin{aligned} \sum_{n_w=1}^{N_w} \widehat{\omega}_{n_w}(y; k_x) \Theta_{n_w}(t) + \mathbf{A} \sum_{n_w=1}^{N_w} \widehat{\omega}_{n_w}(y; k_x) \left(\sum_{m_w=1}^{N_w} c_{n_w m_w} \Theta_{m_w}(t) \right) \\ = \sum_{n_w=1}^{N_w} \widehat{F}_{n_w}(y; k_x) \left(\sum_{m_w=1}^{N_w} c_{n_w m_w} \Theta_{m_w}(t) \right), \end{aligned} \quad (9.19)$$

Using the orthogonality of the basis vectors, the equation is now rewritten as:

$$\widehat{\omega}_{n_w}(y; k_x) + \mathbf{A} \sum_{m_w=1}^{N_w} c_{n_w m_w} \widehat{\omega}_{m_w}(y; k_x) = \sum_{m_w=1}^{N_w} c_{n_w m_w} \widehat{F}_{m_w}(y; k_x). \quad (9.20)$$

If we were dealing with the Fourier-based equations $c_{n_w m_w} = i n_w \delta_{n_w m_w}$. The summations in (9.20) thereby drop-off giving independent equations for each n_w . This is not true for the case of all bases, such as a wavelet bases, where the response at one particular wavelet Θ_{n_w} cannot be isolated from the responses at the other wavelets. In matrix form, this equation will therefore become:

$$\begin{aligned} \begin{bmatrix} \widehat{\omega}_1(y; k_x) \\ \widehat{\omega}_2(y; k_x) \\ \widehat{\omega}_3(y; k_x) \\ \vdots \end{bmatrix} + \underbrace{\begin{bmatrix} \mathbf{A} & 0 & 0 & \dots \\ 0 & \mathbf{A} & 0 & \dots \\ 0 & 0 & \mathbf{A} & \dots \\ \vdots & \vdots & \vdots & \ddots \end{bmatrix}}_{\widehat{\mathbf{A}}(y, n_w; k_x)} \underbrace{\begin{bmatrix} c_{11} \mathbf{I} & c_{12} \mathbf{I} & c_{13} \mathbf{I} & \dots \\ c_{21} \mathbf{I} & c_{22} \mathbf{I} & c_{23} \mathbf{I} & \dots \\ c_{31} \mathbf{I} & c_{32} \mathbf{I} & c_{33} \mathbf{I} & \dots \\ \vdots & \vdots & \vdots & \ddots \end{bmatrix}}_{\widehat{\mathbf{B}}(y, n_w; k_x)} \begin{bmatrix} \widehat{\omega}_1(y; k_x) \\ \widehat{\omega}_2(y; k_x) \\ \widehat{\omega}_3(y; k_x) \\ \vdots \end{bmatrix} = \\ \underbrace{\begin{bmatrix} c_{11} \mathbf{I} & c_{12} \mathbf{I} & c_{13} \mathbf{I} & \dots \\ c_{21} \mathbf{I} & c_{22} \mathbf{I} & c_{23} \mathbf{I} & \dots \\ c_{31} \mathbf{I} & c_{32} \mathbf{I} & c_{33} \mathbf{I} & \dots \\ \vdots & \vdots & \vdots & \ddots \end{bmatrix}}_{\widehat{\mathbf{B}}(y, n_w; k_x)} \begin{bmatrix} \widehat{F}_1(y; k_x) \\ \widehat{F}_2(y; k_x) \\ \widehat{F}_3(y; k_x) \\ \vdots \end{bmatrix} \end{aligned} \quad (9.21)$$

We are considering the discretized equations with N_y number of grid-points in the y -direction and N_w discrete wavelets. The matrix \mathbf{A} in (9.21) is therefore of size $N_y \times N_y$ and \mathbf{I} represents an identity matrix of the same size. The projection coefficients $c_{n_w m_w}$

are scalars. The matrices $\widehat{\mathbf{A}}(y, n_w; k_x)$ and $\widehat{\mathbf{B}}(y, n_w; k_x)$ are therefore of sizes $(N_w N_y) \times (N_w N_y)$, and the vectors $\widehat{\omega} = [\widehat{\omega}_1, \widehat{\omega}_2, \widehat{\omega}_3, \dots, \widehat{\omega}_{N_w}]$ and $\widehat{F} = [\widehat{F}_1, \widehat{F}_2, \widehat{F}_3, \dots, \widehat{F}_{N_w}]$ are each of size $N_y N_w$. Using these definitions, we can write the wavelet-based linearized equation as:

$$\widehat{\omega}(y, n_w; k_x) + \widehat{\mathbf{A}}(y, n_w; k_x) \widehat{\omega}(y, n_w; k_x) = \widehat{\mathbf{B}}(y, n_w; k_x) \widehat{F}(y, n_w; k_x) \quad (9.22)$$

To obtain the state-vector $\widehat{\mathbf{q}}(y, n_w; k_x) = (\widehat{u}(y, n_w; k_x), \widehat{v}(y, n_w; k_x))$, we will introduce an output-matrix $\widehat{\mathbf{C}}$ such that

$$\widehat{\mathbf{q}}(y, n_w; k_x) = \widehat{\mathbf{C}}(y, n_w; k_x) \widehat{\omega}(y, n_w; k_x). \quad (9.23)$$

The matrix $\widehat{\mathbf{C}}$ can also be used to ‘mask’ the resolvent. For instance, in the upcoming sections, we will compute the responses at specific values of n_w . By selectively including and excluding rows of the matrix $\widehat{\mathbf{C}}$ we can mask the response such that we obtain responses exclusively at a particular n_w .

From this point, the procedure to obtain the resolvent operator follows [McKeon & Sharma \(2010\)](#). Rearranging (9.22) gives us:

$$\widehat{\mathbf{q}}(y, n_w; k_x) = \underbrace{\widehat{\mathbf{C}} \left[\mathbf{W}^{1/2} (I + \widehat{\mathbf{A}})^{-1} \mathbf{W}^{-1/2} \right] \widehat{\mathbf{B}}}_{\widehat{\mathbf{H}}(y, n_w; k_x)} \widehat{F}(y, n_w; k_x), \quad (9.24)$$

Here $\widehat{\mathbf{H}}(y, n_w; k_x)$ represents the resolvent operator. If a non-uniform grid is used to discretize y , the weight matrix \mathbf{W} will contain the weights corresponding to the grid. In this study we employ a Fourier grid with $N = 51$ grid points, resulting in $\mathbf{W} = \mathbf{I}$. Similar to our approach for WPOD (see §5.1), here the Daubechies 1 wavelets serve as the basis vectors Θ_{n_w} , with a time window of $T = 200$ and a time-step of $dt = 1$.

9.2. Wavelet-based resolvent and forcing modes

Singular value decomposition is used to analyze the resolvent operator $\widehat{\mathbf{H}}(y, n_w; k_x)$

$$\widehat{\mathbf{H}}(y, n_w; k_x) = \sum_{i=1}^{N \times N_w} \psi_i(y, n_w) \sigma_i \phi_i(y, n_w). \quad (9.25)$$

The singular values are arranged in increasing order such that $\sigma_i \geq \sigma_{i+1}$. The left singular vectors $\psi_i(y, n_w)$ represent the resolvent response modes and the right singular vectors $\phi_i(y, n_w)$ represent the resolvent forcing modes. Essentially, the forcing $\phi_i(y, n_w)$, when put through the resolvent operator, yields a response $\psi_i(y, n_w)$ amplified by σ_i . Both $\psi_i(y, n_w)$ and $\phi_i(y, n_w)$ are functions of the y -direction and the wavelets n_w . The most amplified response is $\psi_1(y, n_w)$ corresponding to σ_1 , and the corresponding most sensitive forcing direction is $\phi_1(y, n_w)$.

First, let us consider resolvent response modes at specific values of n_w . To obtain these modes, we can selectively mask specific rows of the output matrix $\widehat{\mathbf{C}}$ (see (9.23)). For the resolvent, we need to choose a wavenumber in the x -direction k_x . From figure 7, we know that the dominant modes of this flow have $k_x = 1$. Therefore, for illustrating the resolvent modes in figure 11, we obtain modes at $k_x = 1$. (The shearing motions in figure 7 can be obtained as $k_x \approx 0$ modes, which are not shown here for the sake of brevity). Figure 11 shows the resolvent modes for two values of n_w : (i) $n_w = 2$ that corresponds to the quiet region and (ii) $n_w = 22$ that corresponds to the burst event. The percentages in the title of the figure represent the fraction of energy (at that n_w) captured by the respective mode $\psi_i(y, n_w)$ computed as $\sigma_i^2 / \sum_j \sigma_j^2$.

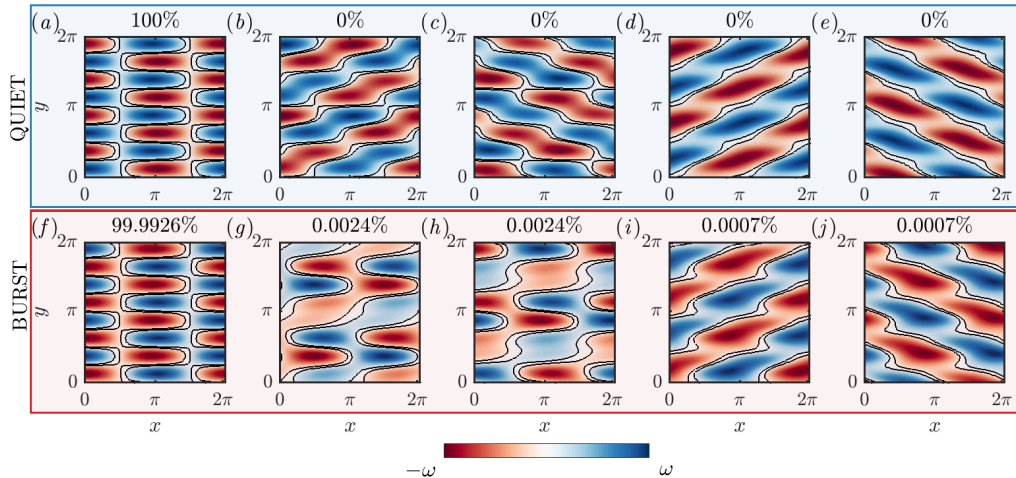


Figure 11: (a) First five resolvent modes corresponding to $n_w = 2$ that contributes to the quiet region, and (b-f) to $n_w = 22$ that contributes to the burst region are shown. The titles show the fraction of energy (at that n_w) captured by the respective mode computed as $\sigma_i^2 / \sum_j \sigma_j^2$ (rounded off to eight decimal places for (a)).

Consider the modes from the quiet region in the first row of figure 11. The first resolvent mode captures almost the full energy at this n_w (the percentage is rounded off to eight decimal places). The mode corresponds to the unstable eigenfunction of the linearized Navier–Stokes equations (see appendix A) (Chandler & Kerswell 2013). Crucially, when compared to the first row of figure 6, the first resolvent mode resembles the first WPOD mode. In §7.1, we found that this first WPOD mode dominates the dynamics of the quiet region in DNS. Therefore, for the quiet region, we can conclude that the model is able to predict the dominant structure. Additionally, the model also recognises the significance of this structure, as indicated by the mode capturing almost all the energy at this n_w .

Now consider the modes for the burst event in the second row of figure 11. The first resolvent mode for this n_w is the same as for the quiet region, representing the unstable eigenfunction and capturing the majority of the energy at this n_w . A similar trend was apparent when considering the WPOD modes in figure 6, where we found that the same modes as in the quiet region were also dominant for the burst event, and captured 60% of the energy of the burst events. In the case of the resolvent modes, however, the quiet region mode captures almost the full energy. Examining the structure of the the sub-optimal resolvent modes, inclined and fragmented versions of the unstable eigenfunction are apparent, reminiscent of the WPOD modes. For instance, compare figure 7(k) with figure 11(g). This suggests that, for the burst events, the resolvent model does capture relevant structures as the sub-optimal modes. However, the model is not able to identify the significance of these sub-optimal modes, as suggested by the percentage of energy captured by them.

9.3. Reconstructing DNS data using wavelet-based resolvent modes

Our purpose in introducing the resolvent here is to find the forcing structures, i.e. the structures in the non-linear terms, that produces the quiet region and burst events. Studies have used the Fourier-based resolvent operators to find the underlying forcing structures that are important in a flow (e.g. Towne *et al.* 2015; Karban *et al.* 2022).

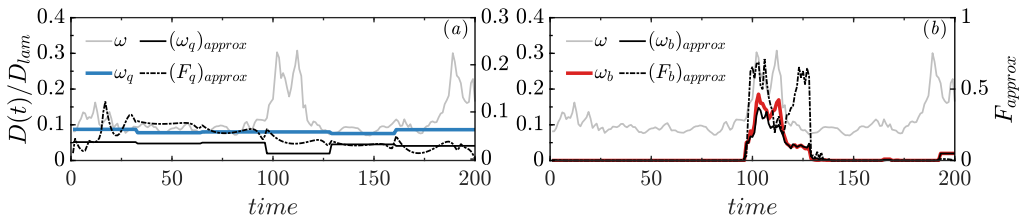


Figure 12: $D(t)/D_{lam}$ computed from the full vorticity data for $k_x = 0, 1, 2, 3$ (grey line) are shown alongside the wavelet-based decomposition of the quiet region (blue line) in (a) and burst events (red line) in (b). The decomposed data are compared to their respective resolvent-based reconstructions (solid black lines). The forcing F_{approx} that generates these responses are also shown (dashed black lines). (The y-axis labels on the right in both (a) and (b) correspond to the forcing).

The right and left singular vectors of the resolvent, ϕ_i and ψ_i , form complete bases. Consequently, any response $\hat{\mathbf{q}}$, and any forcing $\hat{\mathbf{F}}$, that is obtained from data (here from DNS) can be expressed in terms of these basis vectors as

$$\begin{aligned} \hat{\mathbf{F}} &= \sum_{i=1}^{N_y n_w} \chi_i \phi_i & \chi_i &= \sum_{j=1}^{N_w} \int_0^{L_y} \hat{\mathbf{F}}(y, n_w) \phi_i(y, n_w) dy \\ \hat{\mathbf{q}} &= \sum_{i=1}^{N_y N_w} \chi_i \sigma_i \psi_i & \chi_i \sigma_i &= \sum_{j=1}^{N_w} \int_0^{L_y} \hat{\mathbf{q}}(y, n_w) \psi_i(y, n_w) dy. \end{aligned} \quad (9.26)$$

Therefore, given DNS data $\mathbf{q}(y, n_w; k_x)$, we first obtain $\hat{\mathbf{q}}(y, n_w; k_x)$ through a wavelet transform, and thereafter compute $\chi_i \sigma_i$ by projecting $\hat{\mathbf{q}}(y, n_w; k_x)$ onto the resolvent response modes $\psi_i(y, n_w)$. A reduced-order description of the flow can then be obtained by reconstructing the data using a truncated basis

$$\hat{\mathbf{q}}_{approx} = \sum_{i=1}^{N_1} \chi_i \sigma_i \psi_i, \quad (9.27)$$

where N_1 is the number of modes that are retained in the truncated data. The approximate data \mathbf{q}_{approx} is then obtained from an inverse wavelet transform in time and an inverse Fourier transform in the x -direction.

From the obtained product $\chi_i \sigma_i$, we then extract χ_i . The N_1 is chosen such that we eliminate modes which contribute less than 0.1% energy to any particular k_x (i.e. the eliminated modes have $\chi_i \chi_i^* \sigma_i^2$ less than 0.1% of the energy at that k_x). This χ_i is then used to compute the forcing $\hat{\mathbf{F}}_{approx} = \sum_{i=1}^{N_1} \chi_i \phi_i$. The obtained forcing $\hat{\mathbf{F}}_{approx}$ when put through the resolvent operator will give a response $\hat{\mathbf{q}}_{approx}$. In other words, we can find the component of the full forcing $\hat{\mathbf{F}}$ from DNS (i.e. the non-linear term) that is specifically responsible for amplifying the response $\hat{\mathbf{q}}_{approx}$. The forcing F_{approx} can then be obtained from an inverse wavelet transform in time and an inverse Fourier transform in the x -direction. An illustration of this procedure is shown in figure 12, where figures 12(a) and 12(b) shows the vorticity ω from DNS decomposed into the quiet (blue) and the burst (red) regions, respectively. The corresponding resolvent based reconstructions ω_{approx} (black solid lines) are also shown ($(\omega_q)_{approx}$ and $(\omega_b)_{approx}$ represent the reconstructions of the quiet region and the burst events, respectively). Additionally, the forcing F_{approx} that generate these responses are shown (black dashed lines) in these figures. Using WRA,

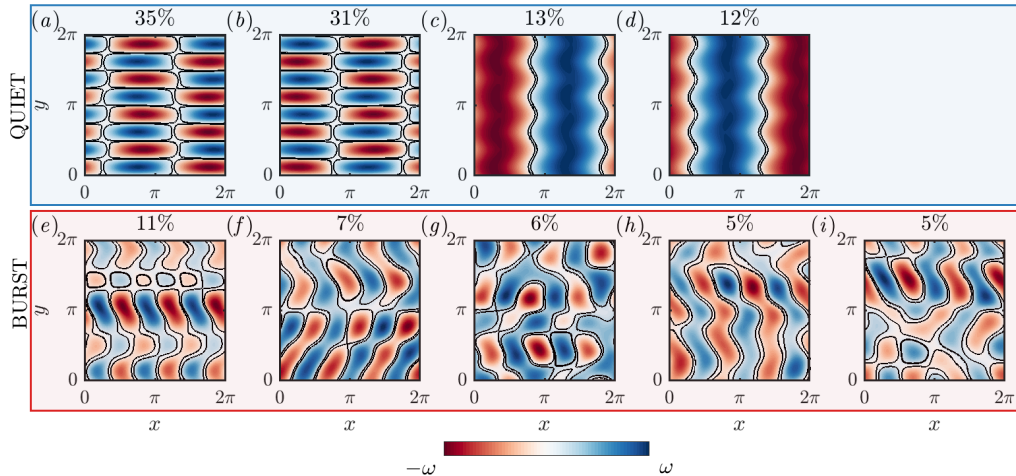


Figure 13: (a) The first few POD modes obtained from the forcing corresponding to the resolvent reconstruction of (a-e) the quiet regions and (f-j) the burst events.

we have therefore constructed forcing $(F_q)_{approx}$ and $(F_b)_{approx}$ that separately generate the quiet region and the burst events, respectively.

9.4. Coherent structures of the forcing

Our aim is to identify the coherent structures in the forcing that generates the quiet region and the burst events. In order to find these coherent structures, we first start by using the resolvent to reconstruct the flow field as illustrated in figure 12, and thereby obtain the corresponding forcing. This reconstruction is performed for M different realisations of the quiet region and the burst events (here $M = 50$). Consequently, we obtain M realisations of resolvent-based vorticity reconstructions $(\omega_{approx,1}(x, y, t), \omega_{approx,2}(x, y, t), \dots, \omega_{approx,M}(x, y, t))$ and the corresponding forcing $(F_{approx,1}(x, y, t), F_{approx,2}(x, y, t), \dots, F_{approx,M}(x, y, t))$. It is important to note that, for the reconstructions done here, $k_x = (0, 1, 2, 3)$ wavenumbers in the x -direction are utilised. Subsequently, to extract the coherent structures, we perform a POD on the M realisations of the forcing. This involves constructing a data matrix P :

$$P = [F_{approx,1}(x, y, t_1), F_{approx,1}(x, y, t_2), \dots, F_{approx,1}(x, y, T), \\ F_{approx,2}(x, y, t_1), F_{approx,2}(x, y, t_2), \dots, F_{approx,2}(x, y, T), \dots]. \quad (9.28)$$

A singular value decomposition of the data matrix P gives us the POD modes. We obtain such POD modes for the quiet region and the burst events.

The top row of figure 13 shows the first few forcing POD modes obtained for the quiet region. The titles of these figures show the percentage of energy that is captured by the mode. Notably, the first two modes capture a majority of the energy, and the modes resemble the unstable eigenfunction itself. This again suggests that the dominant amplification mechanism is a normal-mode mechanism, where the forcing and response modes can be expected to be structurally similar. Interestingly, modes 3 and 4 resemble the dominant resolvent forcing to the unstable eigenfunction (see appendix A), which suggests that there is a second route through which the unstable eigenfunction can be amplified. We can also obtain the forcing POD modes for the burst events, and the first five of these modes are shown in the bottom row of figure 13. Notably, inclined structures dominate the forcing to the burst events.

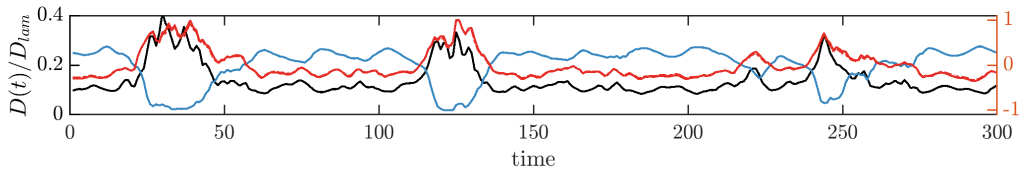


Figure 14: Tracking forcing structures for the quiet region using γ^q (blue line) and for the burst events using γ^b (red line).

10. Predicting burst events using forcing coherent structures - Method 3

Now that we have identified the coherent structures in the forcing that generates the quiet regions and the burst events, we will track them in a time-series obtained from the flow. More specifically, our interest is in analysing how the contributions of these structures to the non-linear terms of the flow evolve with time. This will then enable us to introduce the WRA-based method 3 for predicting the burst events, where we will use these forcing coherent structures. We have two sets of forcing coherent structures: (i) let F_q represent the modes corresponding to the quiet region, with each mode $\phi_i^q(x, y)$ having POD energy $\tilde{\mathcal{E}}_i^q$, and (ii) F_b the modes for the burst event with each mode $\phi_i^b(x, y)$ having POD energy $\tilde{\mathcal{E}}_i^b$. Both F_q and F_b contain $M \times N_t$ modes, where M is the number of resolvent reconstructions used (here $M = 50$) and N_t is the number of time-snapshots of DNS data in each realisation (here $N_t = 200$). To simplify computation, here we ignore modes that cumulatively contribute less than 1% energy (i.e. POD modes k with $\sum_{i=k}^M \tilde{\mathcal{E}}_i^q / \sum_{j=0}^M \tilde{\mathcal{E}}_j^q < 1$). At each time t , we aim to assess the presence of the structures in F_q and F_b in the non-linear terms $F(x, y, t)$ obtained from the flow.

For this purpose, we follow the methodology laid out in §7.1, with $\mathbf{q}(x, y, t)$ now taken to be the non-linear terms $F(x, y, t)$ obtained from DNS. As explained in §7.1, we will obtain $\gamma^q(t)$ which is the weighted average of the coherence of the modes in F_q with each point in the time-series $F(x, y, t)$. Equivalently, we will also obtain $\gamma^b(t)$ for the modes in F_b . As in §7.1, we are interested in the trends of $\gamma^q(t)$ and $\gamma^b(t)$, and not the actual values. Figure 14 therefore shows the normalised (by the maximum) profiles of $\gamma^q(t)$ and $\gamma^b(t)$. We see that $\gamma^q(t)$ and $\gamma^b(t)$ follow distinctive trends during a burst event, with $\gamma^q(t)$ (blue line) decreasing and $\gamma^b(t)$ (red line) increasing. The trends of $\gamma^q(t)$ and $\gamma^b(t)$ can therefore be used for predicting the burst event.

Like in §8, here we will define a predictor $\lambda = \gamma^q(t) - \gamma^b(t)$. Figure 15 shows the evolution of this predictor for three different time-windows. (As in §8, here λ is normalised by the minimum and the maximum values obtained within the time window $t = 0 - 15000$.) Using the same method as in §8, we again choose a threshold λ_t . The times where λ is below λ_t are identified as predictions of the burst regions, and the red shaded regions in figure 15 denotes the prediction of the burst regions. These prediction times are compared to the green dashed lines, which denote the predictions obtained using the WPOD structures in §8. First, we note that, by tracking the forcing structures, we are indeed able to obtain predictions of the burst event. These prediction times are always improvements over the WPOD method. We also note that false positives are obtained using this method as well (e.g. $t \approx 40$ in figure 15(c)).

10.1. Varying the threshold of the predictor

The prediction methods discussed rely on a predictor going below a threshold value. Therefore the predictions will vary with this choice of the threshold. The thresholds were

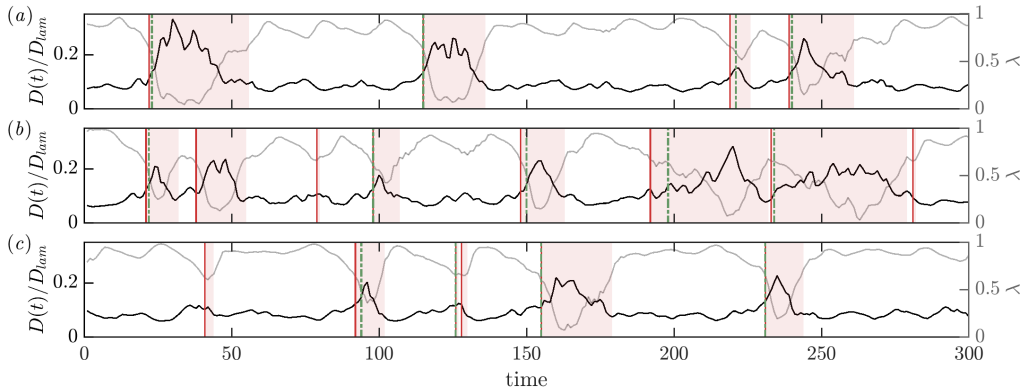


Figure 15: (a) Predictions obtained from tracking forcing structures identified through WRA (prediction method 3). The red shaded regions indicate the identified burst regions where the predictor (grey line) has $\lambda < \lambda_t$. Vertical red lines mark the onset of these burst regions, representing the predictions of the burst event from the WRA-based method. Predicted times are compared to those obtained from the WPOD-based method 2 (green dashed-dot lines).

chosen as 0.95 times the mean of the predictor λ minus the variance, where these statistics were computed specifically for time instances corresponding to the quiet regions (see §8). Figure 16 illustrates how varying this coefficient 0.95 impacts predictions obtained from the WPOD-based method 2 in green and WRA-based method 3 in red.

Two quantities are shown in figure 16. First, in figure 16(a), the obtained average improvement in prediction times (denoted by τ) compared to method 1. (Note, τ is shown in units of $\sqrt{L_y}/2\pi\zeta$ where ζ is the amplitude of forcing per unit mass). Second, in figure 16(b), the percentage of predictions that are false positives (denoted by FP%). To compute this FP%, a false positive is defined as a prediction where $D(t)/D_{lam}$ of the flow does not go above 0.15 (e.g. $t \approx 40$ in figure 15(c)). Both quantities are computed from data within a time-window with $T = 4000$ and $dt = 1$ outside of the N_e realisations used for WPOD. To simplify discussion, the threshold of 0.15 for method 1 is kept fixed throughout this work. The vertical dashed-dot black lines in figure 16(a) represents 0.95 chosen for figures 10 and 15.

From figure 16 we see that, as expected, for both methods, the prediction times improve as we increase the threshold. However, this comes at the cost of an increase in the false positives obtained, and this increase is more pronounced for the WRA-based method. More interestingly, compared to the WPOD-based method, the WRA-based method yields improved prediction times across all threshold values. On average, the WRA-based method gives an improvement of 0.8 time-units when compared to the WPOD-based method, calculated as the average distance between the red and black lines in figure 16(a). For instance, at 0.95, the FP% obtained from the WPOD-based method is approximately 11%, while that from the WRA-based method is 18%. However, the improvements in prediction times τ increase from 3.25 time unit for the WPOD-based method to 4.0 time units for the WRA-based method. (Appendix B shows how this prediction performance changes for a different choice of wavelets, Daubechies 2 instead of the Daubechies 1 used here.)

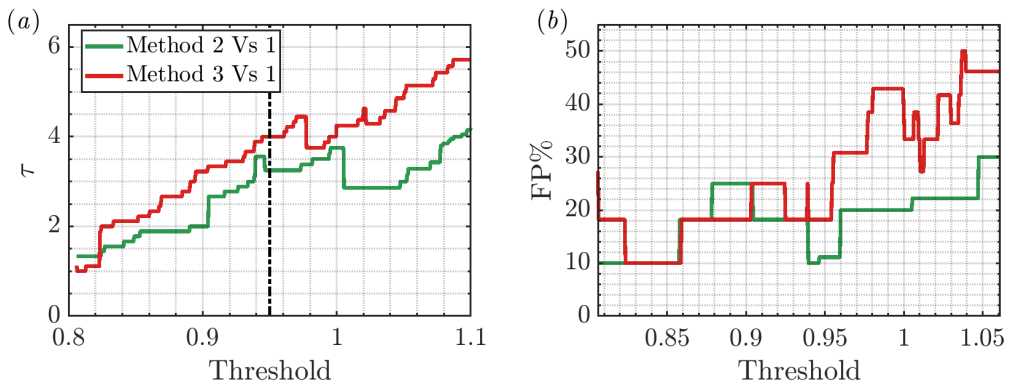


Figure 16: (a) The average improvement in prediction times in comparison to the energy tracking method 1 for WPOD-based method 2 (green) and WRA-based method 3 (red) are shown as a function of the threshold defined for predictors. (b) The percentage of the obtained predictions that are false positives are also shown for the two methods.

11. A discussion of the predictions obtained

So far we have looked at two different methods to predict intermittent events in a flow: (i) tracking the coherent structures obtained from WPOD and (ii) tracking the forcing structures that generate these coherent structures through the resolvent operator. We illustrated these methods using the 2-D Kolmogorov flow, which is governed by the unstable eigenfunction of the linearized Navier–Stokes equations. The quiet region of this flow is dominated by this unstable eigenfunction and the burst events seem to happen because of a disruption of this structure. In other words, there is a single eigenfunction of the linearized Navier–Stokes equations that seems to govern the flow. The energy amplification mechanism in this flow therefore is likely a normal-mode amplification mechanism. In this scenario, the resolvent analysis shouldn’t actually be expected to give a significant time-delay between the forcing and the response.

Contrary to this, we could analyze a flow where the energy amplification occurs due to non-normal mechanisms, such as for instance the streak-generation in channel flows. In this case the forcing will have a time-delay from the response. This is due to the transient growth mechanisms that causes energy amplification in non-normal flows (e.g. [Trefethen et al. 1993](#); [Schmid 2007](#)). In this case, the forcing structure method that is described here will likely provide better prediction times in comparison to the WPOD structure based method. Comparing the two methods for such non-normal flows is therefore an important future direction of work.

12. Conclusions

In this study, we used wavelet-based methods to understand, and therefore predict, high-energy intermittent bursting events in flows. The flow considered was a 2D Kolmogorov flow at a Reynolds number of $Re = 40$ forced by a sinusoidal body forcing with wavenumber $n = 4$. In this regime, for a majority of the time, the flow remains quiet with minor oscillations in energy. This quiet region is occasionally interrupted by intermittent high-energy burst events. The focus was on finding distinctive flow patterns for the quiet regions and the burst events, and thereafter track these structures to obtain predictions of oncoming burst events.

Due to the time-localized nature of the burst events, Fourier-based methods proved

inefficient in capturing them (figure 2). Consequently, we used wavelet-based methods (figure 5). Two wavelet-based techniques were employed: (i) wavelet-based Proper Orthogonal Decomposition (WPOD) to distinguish the dominant flow patterns of the quiet region and burst events (figure 7), and (ii) wavelet-based resolvent analysis (WRA) to identify forcing structures that generate the quiet region and burst events (figure 13). Subsequently, coherence-based methods were used to track these structures in the evolving time-series of the flow. This approach yielded two effective strategies to predict oncoming burst events: (i) the WPOD-based method 2 involved tracking the flow patterns obtained from WPOD (figure 10) and (ii) the WRA-based method 3 involved tracking the forcing-patterns obtained from WRA (figure 15). These predictions were then compared to those obtained from the more straightforward Method 1, which focused on tracking the energy of the flow (figure 1).

The WPOD analysis revealed three dominant flow patterns (figure 7): (i) the unstable eigenfunction of the linearized Navier–Stokes equations that dominates the quiet region, (ii) shearing structures, also present in the quiet region, and (iii) fragmented or distorted versions of the unstable eigenfunction, crucial during burst events. Tracking these modes revealed that the shearing motions move out of phase with the flow due to the unstable eigenfunction. Moreover, the presence of the unstable eigenfunction decreases during the burst events, while the presence of the fragmented versions of the unstable eigenfunction increases. Based on these observations, we hypothesise that in the 2-D Kolmogorov flow, shearing motions distort the flow due to the unstable eigenfunction, leading intermittently to burst events. Identifying regions where the flow due to the fragmented or distorted eigenfunctions dominates over the flow due to the eigenfunction itself allowed us to develop the WPOD-based method 2 for predicting oncoming burst events.

Thereafter, using resolvent analysis, we identified the forcing structures that generate the unstable eigenfunction, dominant in the quiet region, as well as inclined forcing structures, dominant during the burst events. Identifying instances when the burst event forcing structures dominate over the quiet region structures led to the development of the WRA-based method 3 of predicting oncoming burst events. Notably, both the WPOD-based and the WRA-based methods were able to predict oncoming burst events and, on average, demonstrated improved prediction times over method 1. However, false positives, where a burst event is predicted while none occurs in the flow, were observed for both methods with the WRA-based method more prone than the WPOD-based method (figure 16). On the other hand, the WRA-based method gives improved prediction times over the WPOD-based method (figure 16), thereby suggesting that tracking forcing structures might be a more efficient prediction strategy.

The initial expectation was that the forcing-based WRA prediction Method 3 would greatly outperform the WPOD-based Method 2. However, for the 2D Kolmogorov flow, while Method 3 does yield improved predictions, the extent of these improvements is not as substantial as initially expected. To understand the underlying reasons for this, we can look at linear mechanisms active in the flow. The dynamics of the 2D Kolmogorov flow are predominantly governed by the unstable eigenvector of the linearized Navier–Stokes equations. Consequently, the energy amplification mechanism that dominates this flow is likely a normal-mode mechanism. As a result, the appearance of the coherent structures in the flow, and the forcing that generates them, may occur without significant time-delay. In order to evaluate the prediction methods, there is therefore a requirement to compare the methods in flows where non-normal mechanisms are active. A natural progression to this work, therefore, is to evaluate burst events in wall-bounded flows, that arise from the breakdown of streaks generated by non-normal mechanisms (e.g. Jiménez 2018). We hope to report on findings from this line of research in the near future.

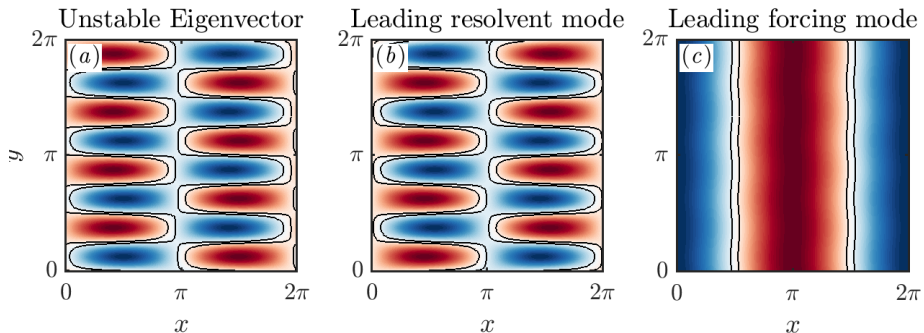


Figure 17: (a) The unstable eigenvector of the linearized Navier–Stokes equations is shown for $k_x = 1$. Also shown are the Fourier-based resolvent (b) response mode and (c) the corresponding forcing mode for a temporal frequency of $\Omega = 0$.

Acknowledgements: The authors would like to thank the Isaac Newton Institute for Mathematical Sciences for support and hospitality during the programme ‘Mathematical aspects of turbulence: where do we stand?’ where part of the work on this paper was undertaken. This was supported by: EPSRC grant number EP/R014604/1. We would also like to thank Dr. Sean Symon for helpful suggestions regarding this work.

Declaration of interests: The authors report no conflicts of interest.

A. Unstable eigenvector of the linearized Navier–Stokes equations

Figure 17(a) shows the unstable eigenvector of the linearized Navier–Stokes equations for $k_x = 1$ obtained from matrix \mathbf{A} in (3.4). The resemblance between the leading WPOD modes obtained in figures 6 and 7 and the unstable eigenvector is evident. Additionally, figure 17 presents the Fourier-based resolvent mode for $k_x = 1$ at temporal frequency $\Omega = 0$. The leading resolvent response mode is shown in 17(b), and this mode is similar to the unstable eigenvector. The corresponding leading forcing mode in 17(c) therefore represents the forcing that captures the unstable eigenvector. The similarity between this forcing mode, and the sub-optimal forcing modes obtained from the WRA method for the quiet region in figure 13 is apparent.

B. Prediction using Daubechies 2 wavelets

In this section, we reproduce the WPOD-based and the WRA-based prediction performance results, but this time using the Daubechies 2 (DB2) wavelets, instead of the Daubechies 1 (DB1) wavelets used in the rest of the manuscript. Figure 18 shows the comparison in figure 16 for predictions using DB2. As in figure 16, two quantities are shown in figure 18. The obtained average improvement in prediction times (denoted by τ) compared to method 1 in figure 18(a), and the percentage of predictions that are false positives (denoted by FP%) in figure 18(b). The lighter coloured lines are reproductions of the corresponding lines in figure 16 (i.e. the predictions using DB1) shown here again for comparison. Using DB2 instead of DB1, we obtain marginally improved (earlier) predictions from the WRA-based method 3. Apart from that, we note that the obtained prediction performances are similar for both DB1 and DB2. This shows that the results are fairly insensitive to the choice of wavelets between DB1 and DB2.

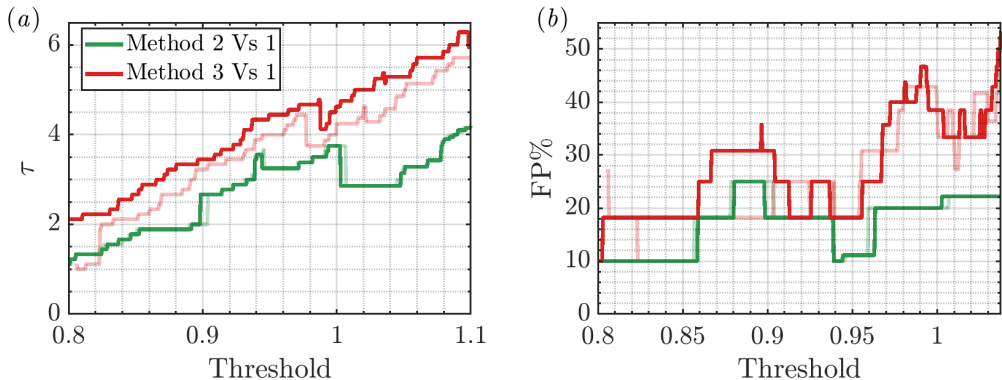


Figure 18: (a) The average improvement in prediction times in comparison to the energy tracking method 1 for WPOD-based method 2 (green) and WRA-based method 3 (red) are shown as a function of the threshold defined for predictors. (b) The percentage of the obtained predictions that are false positives are also shown for the two methods. Here the prediction obtained from the Daubechies 2 wavelets are shown and compared to the predictions obtained in figure 16 using the Daubechies 1 wavelets (reproduced here as the lighter coloured lines).

REFERENCES

- BABAEE, H. & SAPSIS, T. P. 2016 A minimization principle for the description of modes associated with finite-time instabilities. *Proc. R. Soc. Lond. A* **472** (2186), 20150779.
- BALLOUZ, E., DAWSON, S. & BAE, H. J. 2023a Transient growth of wavelet-based resolvent modes in the buffer layer of wall-bounded turbulence. *arXiv preprint arXiv:2312.15465*.
- BALLOUZ, E., LOPEZ-DORIGA, B., DAWSON, S. T. & BAE, H. J. 2023b Wavelet-based resolvent analysis for statistically-stationary and temporally-evolving flows. In *AIAA SCITECH 2023 Forum*, p. 0676.
- BARTHEL, B. & SAPSIS, T. 2023 Harnessing the instability mechanisms in airfoil flow for the data-driven forecasting of extreme events. *arXiv preprint arXiv:2303.07056*.
- BAYINDIR, C. 2016 Early detection of rogue waves by the wavelet transforms. *Phys. Lett. A* **380** (1-2), 156–161.
- BLONIGAN, P. J., FARAZMAND, M. & SAPSIS, T. P. 2019 Are extreme dissipation events predictable in turbulent fluid flows? *Phys. Rev. Fluids* **4** (4), 044606.
- CHANDLER, G. J. & KERSWELL, R. R. 2013 Invariant recurrent solutions embedded in a turbulent two-dimensional Kolmogorov flow. *J. Fluid Mech.* **722**, 554–595.
- DOAN, N. A. K., POLIFKE, W. & MAGRI, L. 2021 Short-and long-term predictions of chaotic flows and extreme events: a physics-constrained reservoir computing approach. *Proc. R. Soc. A* **477** (2253), 20210135.
- DONZIS, D. A. & SREENIVASAN, K. R. 2010 Short-term forecasts and scaling of intense events in turbulence. *J. Fluid Mech.* **647**, 13–26.
- DYSTHE, K., KROGSTAD, H. E. & MÜLLER, P. 2008 Oceanic rogue waves. *Annu. Rev. Fluid Mech.* **40**, 287–310.
- FARAZMAND, M. & SAPSIS, T. P. 2016 Dynamical indicators for the prediction of bursting phenomena in high-dimensional systems. *Phys. Rev. E* **94** (3), 032212.
- FARAZMAND, M. & SAPSIS, T. P. 2017 A variational approach to probing extreme events in turbulent dynamical systems. *Sci. Adv.* **3** (9), e1701533.
- FARAZMAND, M. & SAPSIS, T. P. 2019a Closed-loop adaptive control of extreme events in a turbulent flow. *Phys. Rev. E* **100** (3), 033110.
- FARAZMAND, M. & SAPSIS, T. P. 2019b Extreme events: Mechanisms and prediction. *Appl. Mech. Rev.* **71** (5), 050801.
- FARGE, MARIE 1992 Wavelet transforms and their applications to turbulence. *Annu. Rev. Fluid Mech.* **24** (1), 395–458.

- FARGE, M., PELLEGRINO, G. & SCHNEIDER, K. 2001 Coherent vortex extraction in 3D turbulent flows using orthogonal wavelets. *Phys. Rev. Lett.* **87** (5), 054501.
- FARGE, M. & RABREAU, G. 1988 Transformée en ondelettes pour détecter et analyser les structures cohérentes dans les écoulements turbulents bidimensionnels. *C. R. Acad. Sci. Paris* **307**, 1479–1486.
- FARGE, M., SCHNEIDER, K., PELLEGRINO, G., WRAY, A. A. & ROGALLO, R. S. 2003 Coherent vortex extraction in three-dimensional homogeneous turbulence: Comparison between CVS-wavelet and POD-Fourier decompositions. *Phys. Fluids* **15** (10), 2886–2896.
- FLORYAN, D. & GRAHAM, M. D. 2021 Discovering multiscale and self-similar structure with data-driven wavelets. *Proc. Natl. Acad. Sci.* **118** (1), e2021299118.
- FOX, A. J., CONSTANTE-AMORES, C. R. & GRAHAM, M. D. 2023 Predicting extreme events in a data-driven model of turbulent shear flow using an atlas of charts. *Phys. Rev. Fluids* **8** (9), 094401.
- GUPTA, S., SHANBHOGUE, S., SHIMURA, M., GHONIEM, A. & HEMCHANDRA, S. 2022 Impact of a centerbody on the unsteady flow dynamics of a swirl nozzle: Intermittency of precessing vortex core oscillations. *J. Eng. Gas Turbines Power* **144** (2), 021014.
- GUTH, S. & SAPSIS, T. P. 2019 Machine learning predictors of extreme events occurring in complex dynamical systems. *Entropy* **21** (10), 925.
- HWANG, Y. & COSSU, C. 2010 Linear non-normal energy amplification of harmonic and stochastic forcing in the turbulent channel flow. *J. Fluid Mech.* **664**, 51–73.
- JIMÉNEZ, J. 2018 Coherent structures in wall-bounded turbulence. *J. Fluid Mech.* **842**, P1.
- KARBAN, U., MARTINI, E., CAVALIERI, A. V. G., LESSHAFFT, L. & JORDAN, P. 2022 Self-similar mechanisms in wall turbulence studied using resolvent analysis. *J. Fluid Mech.* **939**, A36.
- LUMLEY, J. L. 1967 The structure of inhomogeneous turbulent flows. *Atmospheric turbulence and radio wave propagation* pp. 166–178.
- LUMLEY, J. L. 1970 *Stochastic tools in turbulence*. Academic Press.
- MCKEON, B. J. & SHARMA, A. S. 2010 A critical-layer framework for turbulent pipe flow. *J. Fluid Mech.* **658**, 336–382.
- MENEVEAU, C. 1991 Analysis of turbulence in the orthonormal wavelet representation. *J. Fluid Mech.* **232**, 469–520.
- MOARREF, R., SHARMA, A. S., TROPP, J. A. & MCKEON, B. J. 2013 Model-based scaling of the streamwise energy density in high-Reynolds number turbulent channels. *J. Fluid Mech.* **734**, 275–316.
- MORRA, P., NOGUEIRA, P. A. S., CAVALIERI, A. V. G. & HENNINGSON, D. S. 2021 The colour of forcing statistics in resolvent analyses of turbulent channel flows. *Journal of Fluid Mechanics* **907**.
- NEELIN, J. D., BATTISTI, D. S., HIRST, A. C., JIN, F.-F., WAKATA, Y., YAMAGATA, T. & ZEBIAK, S. E. 1998 ENSO theory. *J. Geophys. Res.* **103** (C7), 14261–14290.
- PAGE, J., BRENNER, M. P. & KERSWELL, R. R. 2021 Revealing the state space of turbulence using machine learning. *Phys. Rev. Fluids* **6** (3), 034402.
- PYRAGAS, V. & PYRAGAS, K. 2020 Using reservoir computer to predict and prevent extreme events. *Phys. Lett. A* **384** (24), 126591.
- QI, D. & MAJDA, A. J. 2020 Using machine learning to predict extreme events in complex systems. *Proc. Natl. Acad. Sci.* **117** (1), 52–59.
- RACCA, A. & MAGRI, L. 2022 Data-driven prediction and control of extreme events in a chaotic flow. *Phys. Rev. Fluids* **7** (10), 104402.
- REN, J., MAO, X. & FU, S. 2021 Image-based flow decomposition using empirical wavelet transform. *J. Fluid Mech.* **906**, A22.
- ROBINSON, S. K. 1991 Coherent motions in the turbulent boundary layer. *Annu. Rev. Fluid Mech.* **23** (1), 601–639.
- ROWLEY, C. W. & DAWSON, S. T. M. 2017 Model reduction for flow analysis and control. *Annu. Rev. Fluid Mech.* **49**, 387–417.
- RUDY, S. H. & SAPSIS, T. P. 2022 Prediction of intermittent fluctuations from surface pressure measurements on a turbulent airfoil. *AIAA J.* **60** (7), 4174–4190.
- SAPSIS, T. P. 2021 Statistics of extreme events in fluid flows and waves. *Annu. Rev. Fluid Mech.* **53**, 85–111.

- SCHMID, P. J. 2007 Nonmodal stability theory. *Annu. Rev. Fluid Mech.* **39**, 129–162.
- SCHMID, P. J. 2022 Dynamic mode decomposition and its variants. *Annu. Rev. Fluid Mech.* **54**, 225–254.
- SCHMID, P. J., GARCÍA-GUTIERREZ, A. & JIMÉNEZ, J. 2018 Description and detection of burst events in turbulent flows. In *J. Phys.: Conf. Ser.*, , vol. 1001, p. 012015. IOP Publishing.
- SCHMIDT, O. T. & SCHMID, P. J. 2019 A conditional space–time POD formalism for intermittent and rare events: example of acoustic bursts in turbulent jets. *J. Fluid Mech.* **867**, R2.
- SCHNEIDER, K. & VASILYEV, O. V. 2010 Wavelet methods in computational fluid dynamics. *Annu. Rev. Fluid Mech.* **42**, 473–503.
- SRIRANGARAJAN, S., ALLEN, M., PREIS, A., IQBAL, M., LIM, H. B. & WHITTLE, A. J. 2013 Wavelet-based burst event detection and localization in water distribution systems. *J. Signal Process. Syst.* **72**, 1–16.
- TAIRA, K., BRUNTON, S. L., DAWSON, S. T. M., ROWLEY, C. W., COLONIUS, T., MCKEON, B. J., SCHMIDT, O. T., GORDEYEV, S., THEOFILIS, V. & UKEILEY, L. S. 2017 Modal analysis of fluid flows: An overview. *AIAA J.* **55** (12), 4013–4041.
- TOWNE, A., COLONIUS, T., JORDAN, P., CAVALIERI, A. V. & BRES, G. A. 2015 Stochastic and nonlinear forcing of wavepackets in a Mach 0.9 jet. In *AIAA Paper*, p. 2217.
- TOWNE, A., LOZANO-DURÁN, A. & YANG, X. 2020 Resolvent-based estimation of space–time flow statistics. *J. Fluid Mech.* **883**.
- TOWNE, A., SCHMIDT, O. T. & COLONIUS, T. 2018 Spectral proper orthogonal decomposition and its relationship to dynamic mode decomposition and resolvent analysis. *J. Fluid Mech.* **847**, 821–867.
- TREFETHEN, L. N., TREFETHEN, A. E., REDDY, S. & DRISCOLL, T. A. 1993 Hydrodynamic stability without eigenvalues. *Science* **261**, 578–584.
- WAN, Z. Y., VLACHAS, P., KOUMOUTSAKOS, P. & SAPSIS, T. 2018 Data-assisted reduced-order modeling of extreme events in complex dynamical systems. *PLoS ONE* **13** (5), e0197704.
- YEUNG, P. K., ZHAI, X. M. & SREENIVASAN, K. R. 2015 Extreme events in computational turbulence. *Proc. Natl. Acad. Sci.* **112** (41), 12633–12638.